Science Advances
AAAS

Supplementary Materials for

Organic carbon dry deposition outpaces atmospheric processing with unaccounted implications for air quality and freshwater ecosystems

John Liggio *et al.*

Corresponding author: John Liggio, john.liggio@ec.gc.ca; Paul Makar, paul.makar@ec.gc.ca; Shao-Meng Li, shaomeng.li@pku.edu.cn; Drew R. Gentner, drew.gentner@yale.edu

Sci. Adv. **11**, eadr0259 (2025)
DOI: 10.1126/sciadv.adr0259

This PDF file includes:

Speciated organic carbon and supporting measurements

Chemical ionization Mass spectrometry

Oxidized organic gases (and a subset of individual speciated hydrocarbons) were measured using both a Proton Transfer Time-of-Flight Mass spectrometer (PTR-ToF-MS) and Chemical Ionization Time-of-Flight Mass spectrometer (CI-ToF-MS), sampling through a rear facing PFA inlet. The principles of operation for these instruments and their application to atmospheric chemistry studies, including aboard aircraft, have been documented extensively (*90-92*) with additional information relevant to this study described below.

Briefly, the PTR-ToF-MS (Ionicon Analytik GmbH, Austria), which uses H_3O^+ as a primary reagent ion, is sensitive to species whose proton affinity is greater than H_2O, including a number of less oxidized molecules and aromatic compounds. The instrument was configured for this study in a manner identical to a previous oil sands campaign (*43*). The drift tube was held at a constant pressure and temperature of 2.15 mbar and 60 °C, respectively resulting in an E/N of 141 Td. The custom zero system contained a catalytic converter heated to 350 °C with a continuous flow of ambient air at a flow rate of one litre per minute. A permeation tube with 1,2,4-trichlorbenzene was placed at the inlet to improve the sensitivity of the mass calibration for higher masses. The data were processed using Tofware software (Tofwerk AG). The list of calibrated species is provided in Hayden et al. (2022) (*72*). The protonated gases were detected at a time resolution of 1 second and instrumental backgrounds were performed in flight using a custom-built zero-air generating unit. Calibrations were performed using gas standard cylinders (Ionicon, Apel-Reimer and Scott-Marrin; 20 compounds). For observed compounds with no available gas standard, a relative response factor was calculated using the method described in Sekimoto et al. (2017) (*93*) and guided by the work of Koss et al. (2018) (*94*) to define an additional 169 ions.

The CI-ToF-MS (Aerodyne Research Inc.) was operated using iodide as a reagent ion, which is primarily selective for acidic and highly polar species (as I^- clusters), using a configuration described previously (*13*). Calibrations were performed (relative to an internal standard) using commercial and prepared standards for 30 compounds (*72*). For other species without standards, a voltage scanning method was employed post study, as described elsewhere (*13*), to quantify an additional >200 ions. The reagent ion (iodide) for the CI-ToF-MS was generated by passing 2 slpm of UHP N_2 over a methyl iodide permeation tube held at 40 °C. This

flow was then passed through a Polonium 2010 ionizer (NRD P-2031) into the ion molecule reactor (IMR). A flow of humidified N_2 (20 sccm through a stainless steel bubbler) was also added to the IMR in order to keep the ratio of $I(H_2O)^-/I^-$ as constant as possible. The IMR and small segmented quadrupole (SSQ) were pressure controlled to 70 and 1.5 mBar, respectively, using Alicat pressure controllers (PC-EXTSEN). The CIMS sampled from an insulated rearward facing inlet (PFA, 3/8" OD, ¼" ID) at 7 slpm with the instrument taking ~2 slpm and the remaining going to bypass. A flow (50 sccm) of isotopically labelled propanoic acid ($^{13}CC_2H_6O_2$) was constantly added to the inlet during the campaign to track instrument sensitivity. Zeros were produced by passing ambient air through a Pt/Pd catalyst (CD Nova) heated to 350 °C followed by bicarbonate and charcoal scrubbers (United Filtration). The mass resolution at an internal standard peak ($^{13}CC_2H_6O_2I^-$) was ~5400 Th/Th, and the instrument operated with 1 second time resolution, with instrumental backgrounds determined for 20 seconds every 15 minutes by flooding the inlet with 10 slpm of zero air.

Hydrocarbon measurements

Light hydrocarbons (i.e., VOCs) not measured by the PTR-ToF-MS, were quantified with discreet whole-air samples using 1.33-litre electropolished stainless steel canisters (AWAS - Advanced Whole Air Sampler). Canisters were pressurized to approximately 30 psi over a period of approximately 15 seconds, with between 15 and 30 discreet samples collected per flight, at locations upwind and within the plumes from oil sands sources. The samples were analysed as soon as possible after the flight with an analytical system operated at the airport (*72*). The AWAS canisters were then cleaned by a custom-fabricated, automated cleaning system similar to previous methods (*95*), and then used again on subsequent flights. The on-site analytical system consisted of a custom-fabricated Gas Chromatograph (GC) system using cryogenic sample pre-concentration, 2-dimensional gas chromatography, Mass Spectrometric Detection (MS) and Flame Ionization Detection (FID). Details of the analytical system have been described previously (*72*). Compounds were calibrated with primary gas standard mixtures in the ppbv concentration range obtained from Apel-Reimer Environmental Inc. (U.S.A.) and the National Physical Laboratory (UK). Compound retention time drift and potential detector sensitivity changes were monitored and compensated for via daily analysis of a secondary standard gas.

Adsorbent tube sampling and analysis

Intermediate- and semi-volatiIe hydrocarbons were measured with integrated samples that were collected using an offline adsorbent tube sampling assembly mounted in an under-wing pod that has been described in detail elsewhere (*38, 56*). In brief, the adsorbent tubes (a.k.a., cartridges) were packed with a custom mixture of adsorbent materials (i.e., layers of quartz wool, glass beads, Tenax TA, and Carbopack X, which have been shown in past work to collect organic compounds in the I/SVOC range with high efficiency (*96*), and loaded into a system able to sequentially sample up to 10 adsorbent tubes with flow rates through the adsorbent tubes controlled to 250-300 sccm. Samples were generally integrated over the lowest two transects and the highest three transects that typically resulted in two adsorbent tube samples for each virtual flight screen. Offline analysis was conducted using high-resolution mass spectrometry as a function of molecular formula for gas phase species ranging from C_{10} to C_{25} as described in Ditto et al., 2021 (*56*) Samples were thermally desorbed with a GERSTEL TD 3.5+ system, and subsequently separated using an Agilent 7890B gas chromatograph, ionized with atmospheric pressure chemical ionization, and detected with an Agilent 6550 quadrupole time-of-flight mass spectrometer. To quantify the observed complex mixture of I/SVOCs, response factors were calculated using the NIST Reference Gulf of Mexico 2779 Macondo Crude oil reference material for C_{10}-C_{25} species with double bond equivalents ranging from 0-15 (*97*).

Organic aerosol measurements

Organic aerosol mass concentrations were obtained with a high-resolution aerosol mass spectrometer (AMS) (Aerodyne Inc). The AMS provides mass concentrations (ug/m^3) of aerosol species including total organics (OA), NO_3, SO_4 and NH_4 for particles less than ~1 µm. The particles impact a heated surface (600 °C), are vaporized and constituents ionized by 70eV and detected with a time-of-flight mass spectrometer (Tofwerk AG). Several ionization efficiency calibrations were performed prior and during the field campaign and varied by <10 %. Further details of this instrument and its application in the current airborne study are provided elsewhere (*72, 98, 99*).

Snow sampling and dissolved organic carbon (DOC)

Ground-based sites for snow sampling (i.e., in Fig. 1c) were accessed by helicopter and collected >100 m upwind of helicopter exhaust to minimize potential contamination and helicopter downwash. All tools used for sample collection (Teflon and stainless steel) were acid-washed before sampling, and the standard two person "clean hands, dirty hands" sampling protocol was used to minimize potential contamination (*100*). Stainless steel shovels were used to dig snow pits to the ice or ground surface. Custom-made stainless-steel corers and stainless-steel spatulas were used to collect snow into 13 L pre-cleaned high-density polypropylene pails for both water chemistry analysis and determination of snow water equivalence (SWE). To determine SWE, the weight and depth of 10 cores was recorded at each site. In 2017, snowpack samples were also collected at 38 sites under the forest canopy. After collection, the snow was kept frozen until processing at the Canada Centre for Inland Waters (CCIW) in Burlington (Ontario, Canada). Snow samples were processed by first allowing them to melt in their containers in the dark. Both unfiltered and filtered meltwater samples were analyzed for standard water chemistry parameters by the National Laboratory for Environmental Testing (NLET) at CCIW. The NLET is accredited by the Canadian Association for Laboratory Accreditation and ISO 17025 certified.

Gradient flux methods for organic acids from a tailings pond

Fluxes of organic acids (OAc) were estimated using vertical gradient methods at the site of a tailings pond in the oil sands surface mining region, described in detail elsewhere (*101*, *102*). Briefly, high time-resolution continuous gradient measurements of organic acids were made using an acetate ionization chemical ionization mass spectrometer (A-CIMS) which was specifically sensitive to acidic species and utilized in the oil sands region previously (*39*). The instrument sampled from three sampling heights of a vertical tower and were averaged into 30-minute intervals and then combined with 30-minute eddy covariance (EC) data. Fluxes were calculated based on the following equation

$$Flux_{OAc} = -K_c \left(\frac{dc}{dz}\right)_{[\mathrm{OAc}]\mathrm{i}} \quad (1)$$

where K_c is the eddy diffusivity coefficient, derived using EC and gradient methane flux measurements as described in You et al. 2020 (*103*) and dc/dz is the concentration gradient of the organic acids between z=32 m and z=8m. These two heights were selected because their

geometric mean (16 m) approximately coincides with the height where eddy flux (EC) measurements were conducted (18 m). As detailed previously (*103*) the EC flux footprint at 18 m lies predominantly within the edges of the tailings pond under most conditions. Eddy diffusivity coefficients were calculated from the difference in wind speed at 32 m and 8 m combined with the momentum flux determined through eddy covariance at 18 m, and stability-corrected following a previously described method (*104*). Deposition velocities for organic acids ($V_{d,OA}$) were derived using the organic acid flux and the concentration of the organic acid at 18 m, according to the following equation:

$$V_{d,OA} = \frac{Flux_{OA}}{[OA]_{18m}} \quad (2)$$

Additional analysis and modelling descriptions

Secondary organic aerosol (SOA) formation rates

The formation of SOA during flights could potentially interfere with the determination of deposition rates (D_{TGOC}) but was found to be negligible compared to the measured loss of TGOC. This was determined through the analysis of SOA formation rates between screens which were quantified through use of TERRA as described previously for SOA in oil sands related flights (*41*) and for other pollutants (*39, 42*). The approach is similar to the use of TERRA for deposition (above), except using organic aerosol mass differences between screens as measured by the HR-ToF-AMS. Such differences (always in the positive direction), represent the mass of SOA formed between screens. AMS data was not available for all flights. Where possible, the SOA formation rate was subtracted from the transfer rates in the determination of deposition fluxes, or omitted where AMS data was not available. As with other pollutants, extrapolation from the lowest flight track to the surface were performed, with previous analysis having shown that this accounts for the largest uncertainty (~20%) (*105*). An OA background was subtracted from the OA measurements using the edges of the flight screens and between plume data. We note that differences in OA between screens may also include a contribution from particle deposition, such that the amount of SOA estimated to be formed may be a somewhat lower limit to what was actually formed (although particle deposition is known to be slower than gas deposition in most instances). However, given the small positive OA differences between screens (see Fig. 1), compared to the deposited TGOC, particle deposition is highly unlikely to impact

the relative contribution of SOA to the loss of gaseous TGOC observed in Fig. 1. While HR-ToF-AMS data was not available during all flights, the available data (4 flights) indicates that SOA, while large in absolute magnitude, does not introduce bias given its relatively small magnitude compared to TGOC deposition rates.

Monte Carlo simulations of V_d

A Monte Carlo simulation approach was used to estimate the deposition velocity (V_d) for the top 30 measured species shown in Fig. 3a (Table S2), using a simulation method described previously (*37*), adapted here for organic species. The simulation uses a parameterization of dry deposition based on a modified version of the commonly employed resistance approach of Wesely (*9*), with dry deposition velocities described using three resistance terms:

$$V_d = \frac{1}{R_a + R_b + R_c} \qquad (3)$$

where R_a, R_b and R_c represent the aerodynamic, quasi-laminar sublayer and bulk surface resistances respectively. The parameterization used here included the R_a and R_b terms employed in Zhang et al. 2002 (*106*) as this was found to result in the closest model-measurement comparison for SO_2 (*37*), combined with the R_c parameterization employed in the GEM-MACH model (*46*). The effective Henry's Law (H_{eff}) as a function of pH for organics was incorporated into individual terms within R_c, which included mesophyll (R_m), cuticular (R_{cut}) and other exposed surface (R_{cl}) resistances, respectively. For these resistances, acid dissociation constants (K_a) were used to prescribe the H_{eff} as a function of pH:

$$H_{eff} = H_{int} \times \left(1 + \frac{K_a}{10^{-pH}}\right) \qquad (4)$$

where H_{int} represents the intrinsic Henry's Law constant, where both K_a and H_{int} were obtained from the available literature (*107, 108*), or calculated using group contribution methods (*109*). The increase in simulated V_d as a function of pH is attributed to large decreases in the R_c term of the algorithm, such that R_a and R_b become the controlling resistances. Conversely, the simulated V_d for non-dissociating oxygenated species are not affected by pH and remain low (<1 cm s^{-1}) as do the V_d for organic acids when using H_{int} values (equivalent to not allowing dissociation to occur; pH=1). Molecular diffusivities (M_{diff}) for organic species used in the formulation of R_a and R_b were also derived with group contribution methods (https://www3.epa.gov/ceampubl/learn2model/part-two/onsite/estdiffusion-ext.html). Chemical

parameters associated with the simulation of V_d for the 30 species simulated are provided in Table S2. Other prescribed input values for the Monte Carlo simulation were constrained by the range of possible values consistent with the conditions during the aircraft flights as have been described previously (*37*). Calculations for the R_a term were based on meteorological conditions observed during the aircraft flights. The simulation was run for pH values from 1 to 10 across all 30 species, generating a distribution of possible V_d values for each species (and for each pH), based on randomly generated input variables selected from Gaussian distributions with a range of 3 sigma for all input parameters (e.g. Friction velocity, reference height, roughness length, Obukhov length, Schmidt number (see Hayden et al., 2021 (*37*) for the full list). The V_d estimates presented in Fig. 3a represent the mode of the resultant distributions of V_d for each species and pH.

Absorptive deposition estimation approach

Here we use the measured gaseous concentrations of IVOCs/SVOCs during aircraft screen flights to estimate a range of absorptive deposition fluxes, as an assessment of the potential importance of absorption as a deposition pathway. The absorptive partitioning of a hydrocarbon gas to foliage at the surface can be estimated in a manner consistent with absorptive gas-particle partitioning (*10*);

$$\frac{C_{ci}}{C_{g,eq_i}} = \frac{Sub_m f_{OM} 760\, RT}{MW_{OM}\, \varsigma_i\, 10^6\, p^0_{L,i}} \quad (5)$$

Where $\frac{C_{ci}}{C_{g,eq_i}}$ is the ratio of the i'th absorbing organic compound in the condensed phase C_{c_i} to the near-foliage-surface equilibrium gas concentration C_{g,eq_i}, Sub_m is the mass of the substrate available for partitioning (i.e., the alkane waxy layer of coniferous needles, μg m^{-3}), f_{OM} is the fraction of the substrate that is organic material ($f_{OM} \equiv 1$, here), R is the gas constant, T is the temperature (K), MW_{OM} is the average molecular mass of the organic material of the substrate (g mole^{-1}), ς_i is the activity coefficient for the i'th compound (unitless) and $p^0_{L,i}$is the sub-cooled if necessary liquid vapour pressure of the i'th compound (Torr). We make the approximation that $\varsigma_i = 1$ as the relatively high concentration of leaf wax within a forest canopy relative to the condensing species makes this a reasonable assumption.

A source of uncertainty with respect to equation 5 is the extent to which all of the epicuticular wax coating the foliage is available for absorptive partitioning. To address this

question, we consider a range of Sub_m values, from a single monolayer of epicuticular wax Sub_{mm} to the total observation-based value for the dominant foliage of the area (i.e., Jackpines), Sub_{tm}.

The chemical nature of epicuticular waxes has been extensively studied for a large variety of foliage types, including evergreen Jack pine needles (dominant in this study region). They are invariably composed of a large fraction of alkane species (*51*), with molar volumes which can range 290 – 600.5 $cm^3\,mole^{-1}$ (*51*). A single monolayer of substrate mass (Sub_{mm}) is estimated using n-pentacosane (C_{25}) as a representative absorbing medium, since it known to be present in needle waxes (*51*) and has a molar volume (*MV*=453 $cm^3\,mole^{-1}$) in the middle of the expected range, using equation (6):

$$Sub_{mm} = \frac{2 \cdot LAI \cdot MW_{OM} \cdot 10^6}{A_{molecule} \cdot D_{canopy} \cdot N_A} \quad (6)$$

where *LAI* represents the Leaf Area Index (m^2 one-sided leaf area m^{-2} ground area), $A_{molecule}$ the cross sectional area of one substrate molecule (m^2), N_A is Avagadros number, and D_{canopy} the depth of the forest canopy (m). The cross sectional area of a molecule of substrate (i.e., $A_{molecule}$ for n-pentacosane) was calculated (*110*) by assuming a spherical molecule in a close packed hexagonal arrangement as:

$$A_{molecule} = 1.091 \times \left(\frac{MV}{N_A}\right)^{\frac{2}{3}} \quad (7)$$

The estimation of the monolayer substrate mass further assumes that the substrate is evenly distributed throughout the entire canopy layer depth (D_{canopy}) of approximately 22m, on both sides of the available needles. Using parameters in the above equations appropriate for the study region (Table S4), a single monolayer of substrate for the underlying forest, Sub_{mm}, is estimated to be 200 μg m^{-3} (far left side of top x-axis; Fig. 3b).

The upper limit of the substrate mass depends on the total available wax present on the foliage, predominantly Jack Pine needles. A review of the available literature indicates that the mass of epicuticular wax substrate per m^2 of one-sided leaf area varies greatly between tree species ($1x10^4$ - $1x10^7$ μg m^{-2}; median = $4x10^5$ μg m^{-2}) (*111-116*). Coniferous trees tend to possess epicuticular wax coatings on the higher end of the range, with measurements of Jack pine specifically in this region having a wax layer of approximately 4.4 $x10^6$ μg m^{-2} (*117*). Using

this value, the substrate mass associated with the full thickness (Sub_{tm}, μg m^{-3}) is estimated using equation (8)

$$Sub_{tm} = \frac{(4.4\times10^{6})\cdot LAI}{D_{canopy}} \quad (8)$$

resulting in an upper limit to substrate mass of approximately 6.5x10^5 μg m^{-3} (far right side of top x-axis; Fig. 3b).

Sub_{tm} and Sub_{mm} are upper and lower limits to the substrate mass Sub_m of equation (5). These and intermediate values, which represent multiple monolayers, and more than span the range of epicuticular wax seen across different plant species in the literature, are used in equation 5 to derive a range of condensed-phase fractions ($\frac{C_{ci}}{C_{g,eq_i}}$), for the various IVOC/SVOC carbon species observed during the flights. The measured concentrations of gases identified within TGOC were repartitioned using (6) to determine the near-foliage-surface equilibrium concentrations of the gases (C_{g,eq_i}); this effectively considers the partitioning which would occur when a TGOC plume fumigates Jack pine foliage in the region.

Parameters in the above equations are chosen to be representative of the study region and are listed in Table S4, along with the results of sensitivity analysis. Vapor pressures for the measured IVOCs/SVOCs are estimated using the empirical polynomial relationships with carbon number for the types of hydrocarbon classes observed here as described previously (*118*) and ranged between 100 and 10^{-12} Torr. Using another vapour pressure parameterization (SIMPOL; (*119*)), resulted in similar final fluxes (within a factor two).

The deposition flux of the i'th compound (F_i; g m^{-2}), is then derived in a manner analogous to the bidirectional flux for ammonia (*50*) such that,

$$F_i = -\frac{(C_{a_i} - C_{g,eq_i})}{R_a + R_{b_i}} \quad (9)$$

where C_{a_i} and C_{g,eq_i} are the ambient (in-plume) and near-surface-equilibrium concentrations of the gas of interest (μg m^{-3}), and R_a and R_{b_i} are the aerodynamic and quasi-laminar sublayer resistances, as described above. Here, we note that the ambient concentration is repartitioned using eqn. 5 to near-surface and condensed phase values (i.e., $C_{a_i} = C_{c_i} + C_{g,eq_i}$), hence

allowing eqn. 9 to be written as a function of the plume concentration C_{a_i} using equation (5). The calculations carried out here thus estimate the instantaneous flux associated with a plume concentration similar to the aircraft observations for fumigating a Jackpine forest. F_i was calculated specifically for each I/SVOC within a given carbon number bin (Table S3) and summed to provide the carbon number dependent flux of Fig. 3b, for gradually increasing values of Sub_m (red background and left-hand y-axis; darker shades indicate $Sub_m \rightarrow Sub_{tm}$). The total flux in Fig. 3b (blue lines and axes) is derived by summing across all carbon numbers and annualized.

The lifetime associated with absorption to foliage for a fumigating plume $\tau_{dep,abs}$ depends only on R_a, R_b and the length scale over which deposition occurs (D_{canopy}), as shown in equation 10.

$$\tau_{dep.abs} = \frac{R_a + R_b}{D_{canopy}} \quad (10)$$

The R_a and R_b terms, and hence $\tau_{dep,abs}$ for the IVOC/SVOCs here are calculated using diffusion coefficients for individual hydrocarbon species, estimated using EPA On-line Tools for Site Assessment Calculation (https://www3.epa.gov/ceampubl/learn2model/part-two/onsite/estdiffusion-ext.html), and other parameters associated with the underlying forested region (canopy height, roughness length, etc.). The $\tau_{dep,abs}$ for the I/SVOCs in depicted in Fig. 3b is calculated as the average (± standard deviation) across all carbon numbers.

The aim of the absorptive partitioning calculations is to determine the potential for this pathway to contribute to deposition. Several sources of uncertainty must be acknowledged. First, equation 9 implies that if $C_{a_i} > C_{g,eq_i}$, F_i is negative (downwards; deposition), whereas if $C_{a_i} > C_{g,eq_i}$, F_i will be positive (upwards; emissions). This along with the variation in partitioning associated with changing Sub_m (Fig. 3b) implies that some off-gassing of the more volatile components of TGOC may occur when the plume is not passing through the foliage. Second, the term ς_i in equation (5) is formally unity only in the event that $C_{c_i} \ll Sub_m f_{OM}$. Large values of deposited mass will result in non-unity values of ς_i, necessitating a more complex calculation using group methods and an iterative solution approach. Third, co-deposition may

simultaneously occur through more than one pathway; an oxygenated high molecular mass compound may deposit both through a traditional pathway and absorptive deposition.

In theory, the deposition of organic mass could over time, also serve as an absorbing medium. Variations in chemical composition may not be a large modifying factor as a sensitivity analysis (Table S4) indicated that changing the molecular size of the compounds comprising the substrate had only a small impact (i.e., 6-7%) on the resultant absorptive deposition fluxes here. While the quantity of anthropogenic organic (e.g., I/SVOC) species on vegetative surfaces in the area has not been verified, the substrate mass of Fig 3b provides constraints on the amount of depositing mass required for this to be a non-negligible reservoir. If it is assumed that all of the deposition modelled regionally (which ranges from approximately 0.1 to 100 g C m^{-2} yr^{-1} (Fig 5a)) accumulated and becomes the absorbing medium, then a range of substrate mass ($Sub_{I/SVOC}$) (deposited over a year) can be estimated for comparison to that of plant wax substrate derived in Fig 3b:

$$Sub_{I/SVOC} = \frac{Flux_m \cdot MF_{org} \cdot MW_{org} \cdot 10^6}{D_{canopy} \cdot MW_C} \qquad (11)$$

where $Flux_m$ is the modelled regional flux of organic carbon (Fig 5a; g C m^{-2} yr^{-1}), D_{canopy} is the canopy height (20 m), MF_{org} is the mole fraction of carbon in the I/SVOC deposition (C_{16} assumed), MW_C is the molar mass of carbon (12 g $mole^{-1}$), and MW_{org} is the molecular weight of the assumed depositing mass (226 g $mole^{-1}$). This coarse calculation results in an approximate range of potential substrate mass ($Sub_{I/SVOC}$) of $6x10^3$ – $6x10^6$ μg m^{-3}. This estimated range represents an upper limit, as it further assumes that the deposition of C_{16} hydrocarbons was evenly distributed through the canopy depth, and that it is not washed away, taken up by plants/soil, and/or re-partitioned to the atmosphere. Despite the large number of assumptions, under such conditions, the $Sub_{I/SVOC}$ spans a similar range as the estimated substrate mass in Table S4 and Fig 3b (top axis) derived for plant waxes in the region, making it a potentially-relevant absorbing medium in some cases with more substantial accumulation, though as noted in the main text, when varying the absorbing medium by 4 orders of magnitude, our sensitivity analysis showed only ~2x variations in the calculated total I/SVOC deposition flux across that range of substrates.

A future model parameterization for absorptive deposition would thus need to track the mass that has been deposited to the leaf surfaces; the previously deposited mass and the current gas concentration being used to determine $C_{g,eq}$, and hence the magnitude and direction of the flux. For the purposes of this qualitative assessment, the previously deposited mass is assumed to be negligible, such that the flux is always downwards.

Estimating transport timescales above the surface layer via vertical turbulent eddy diffusivity

The atmosphere is inherently heterogeneous across the planetary boundary layer, with turbulent transport varying across the course of the day and with meteorological conditions. These changes can also affect deposition velocity and the theoretical estimates in this study are based on the study conditions for comparison to the flux and deposition velocity observations. Deposition theory governed by R_a, R_b and R_c and associated analysis in this work has indicated that the measured TGOC deposition velocity is most similar to deposition that is independent of substantial surface limitations (Fig 3a, Fig 4c and S5a). This outcome is also consistent with vertical turbulent eddy diffusivity (K_z), also known as K theory or mixing length theory (described below), which represents an alternate approach to estimate the deposition velocity from a given altitude within the mixed boundary layer (e.g., the aircraft location) to the canopy reference height since R_a and R_b are often calculated within the constant flux layer. Similar to other flux parameters, K_z is sensitive to atmospheric conditions and can vary across the height of the atmospheric boundary layer and with time and weather. K_z under neutral atmospheric conditions was calculated to be 14.5 ± 13.0 $m^2\ s^{-1}$, (range: 0.6-32 $m^2\ s^{-1}$) using 4 parameterizations (*120-123*) and the range of observed planetary boundary layer heights on these flights (i.e., 1200-2000 m ASL, 940-1740 m AGL, in 100 m intervals). Using the turbulent diffusion parameterization in $\tau=\Delta x/(2*K_z)$ to approximate the timescale for mixing from higher flight altitudes (e.g., ~1000 m ASL to 40 m AGL), yields an average timescale (from ~1000 m ASL to the canopy reference height (40 m AGL)) and effective deposition velocity of 4.7 hrs and 4.1 cm s^{-1}, which falls in the range of observed overall TGOC deposition velocities (e.g., Figure 3A shaded area & Fig S5A). Turbulent eddy diffusivities across the planetary boundary layer expectedly range considerably across atmospheric conditions and the parameterizations

examined here, but we note that the vertical parameterization used in the WRF model (*123*) give a range of K_z values, transport timescales, and deposition velocities of 9.7-32 $m^2\ s^{-1}$, 2.1-7.1 hrs, and 2.7-9.2 cm s^{-1}, respectively. These timescales, including when combined with the R_a+R_b limited timescales (within the surface layer below the canopy reference height; Fig S5A) span a similar range as the observations (Figure 4A) and support the conclusion of a limited influence of surface resistances. The ranges of both estimated transport timescales through the PBL and of observed TGOC will furthermore vary with slightly to moderately unstable daytime conditions, shortening the transport timescales further, such as the shortest times in Figure 4A. While the reference heights used can influence the calculated and observed deposition velocities and lifetimes, conclusions regarding the importance of deposition relative to other processes remains similar if calculated at 40 m or a flight altitude of 1000 m.

Freshwater DOC flux modelling

The approach to modelling the DOC catchment flux for the domain of Fig. 5 relies upon Thiessen polygons to delineate single-lake hydrological catchment areas for the total lake population (*124*), a database containing landscape characteristics (including observed lake DOC at a subset of catchments), regression kriging to predict and interpolate lake DOC across other geographic areas within the domain which lack data and modelled catchment hydrological outflow using MetHyd (*125*) populated by regional meteorological data. The approach has been shown to adequately predict DOC levels in a nearby region (*60*) and is adapted for the current domain.

The DOC catchment flux estimates for select individual lakes in the region are used to derive Fig. 5b. The lake location data were obtained as polygons from the Canadian National Hydro network in previous work (*60*). A number of these lakes are within 275 km of Fort Mckay (36146 lakes); the entire dataset of 89,947 lakes was used for comparing total DOC and model-estimated TGOC deposition. The total DOC catchment flux (DCF) can be derived with measured DOC concentration data and modelled water flow rates (Q) (*125*):

$$DCF\ (g\ m^{-2}yr^{-1}) = [DOC]\ (g\ L^{-1}) \times\ Q\ (L\ m^{-2}yr^{-1}) \quad (12)$$

GEM-MACH simulated values of TGOC deposition fluxes (DDF) were calculated over the same region at 2.5km grid cell size. Dry deposition flux fractions (DDFF) were generated through

superimposing DDF grid cell polygons on catchments, summing up the net area-weighted DDF value within the catchment polygon, then taking the ratio of this net catchment DDF value to the exiting DOC catchment fluxes (DCF) values. Fig. 5c displays the resulting catchment polygons.

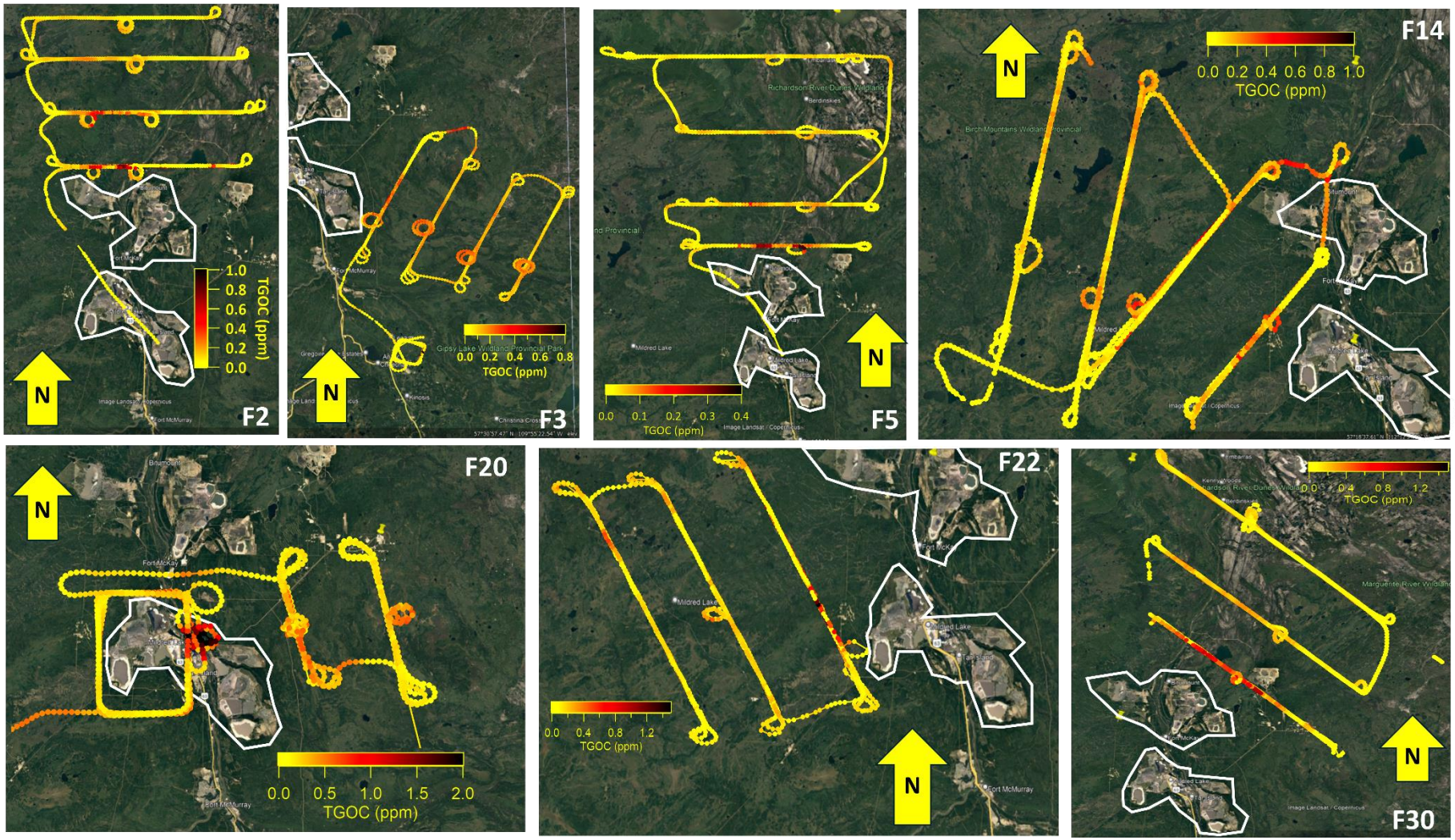

Fig. S1. Flight tracks for the flights used to derive deposition fluxes in the current work colored by TGOC concentration. Approximate oil sands facility locations outlined in white.

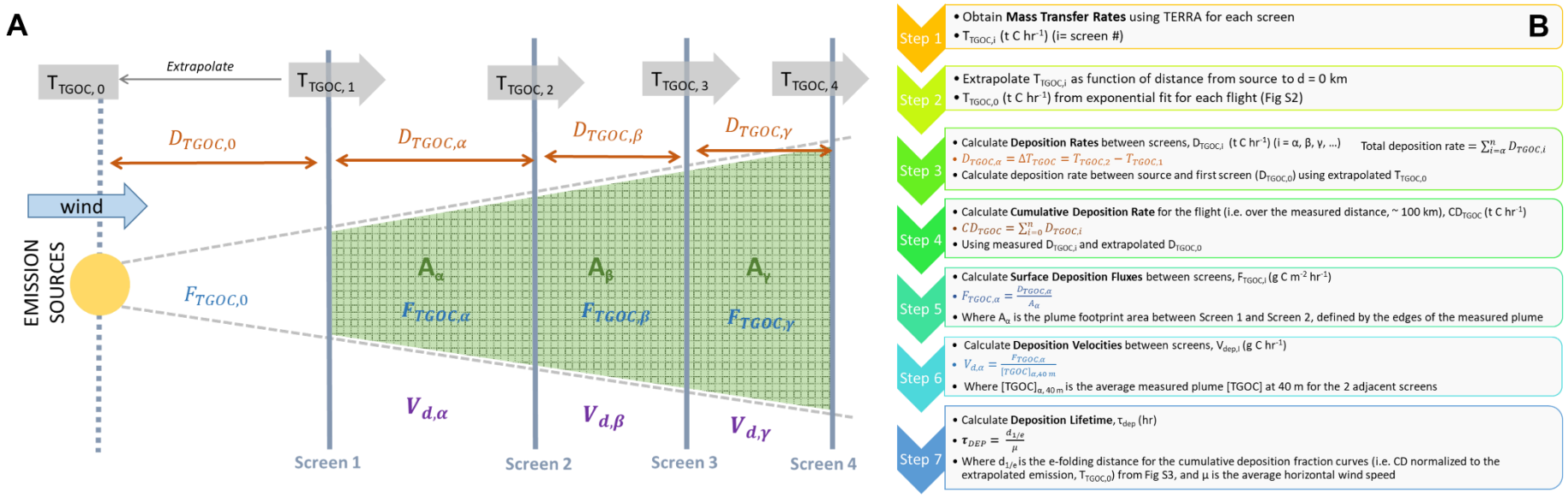

Fig. S2. Estimating deposition parameters from aircraft flights. (**A**) Schematic representation of the various deposition related parameters which can be derived via aircraft measurement of a large scale TGOC plume **(B)** Steps associated with deriving estimates of various deposition parameters. Parameters refer to those defined in panel (A).

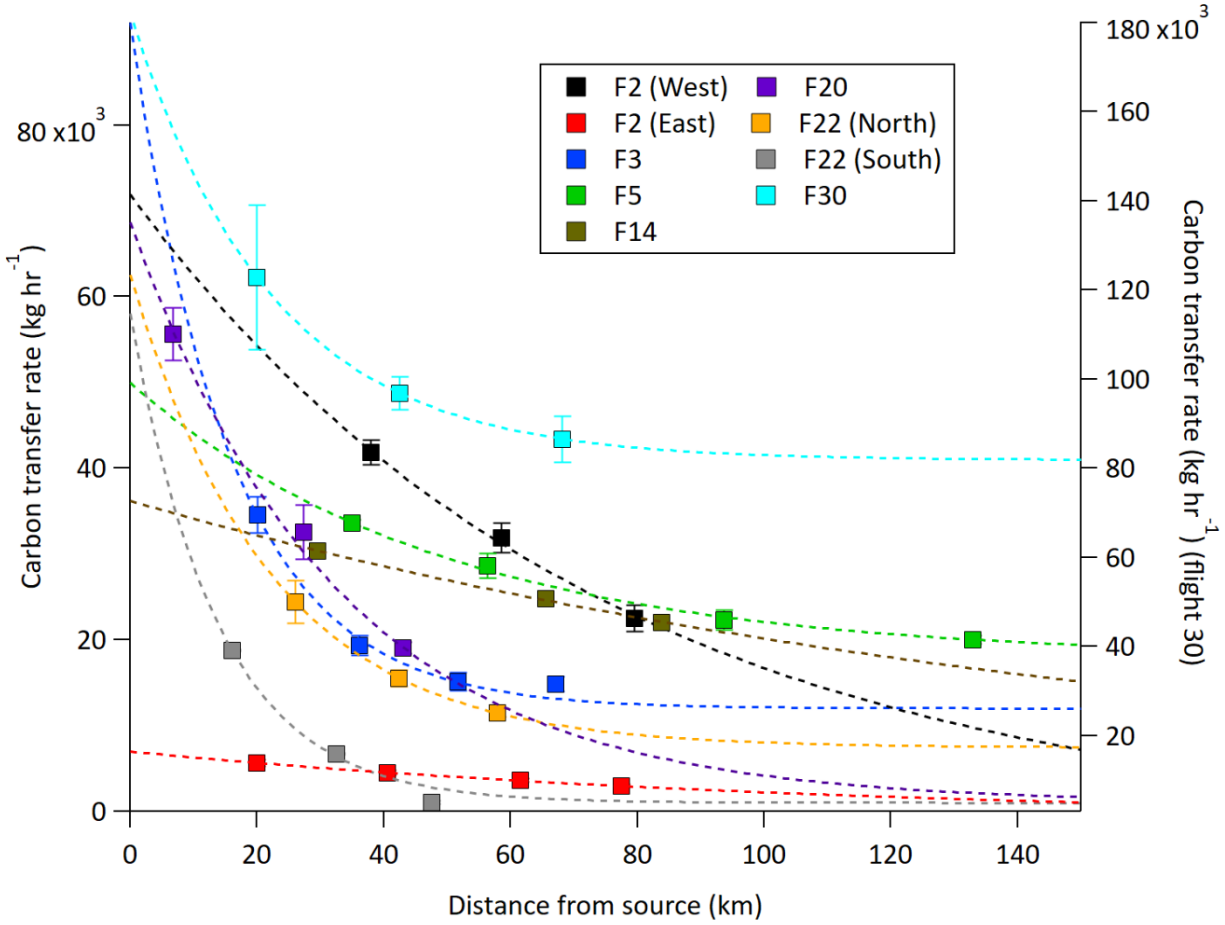

Fig. S3. TGOC mass transfer rates through the TERRA derived virtual screens as a function of source distance. Dashed lines represent exponential fits to the data used in the estimation of the cumulative deposition (CD_{TGOC}).

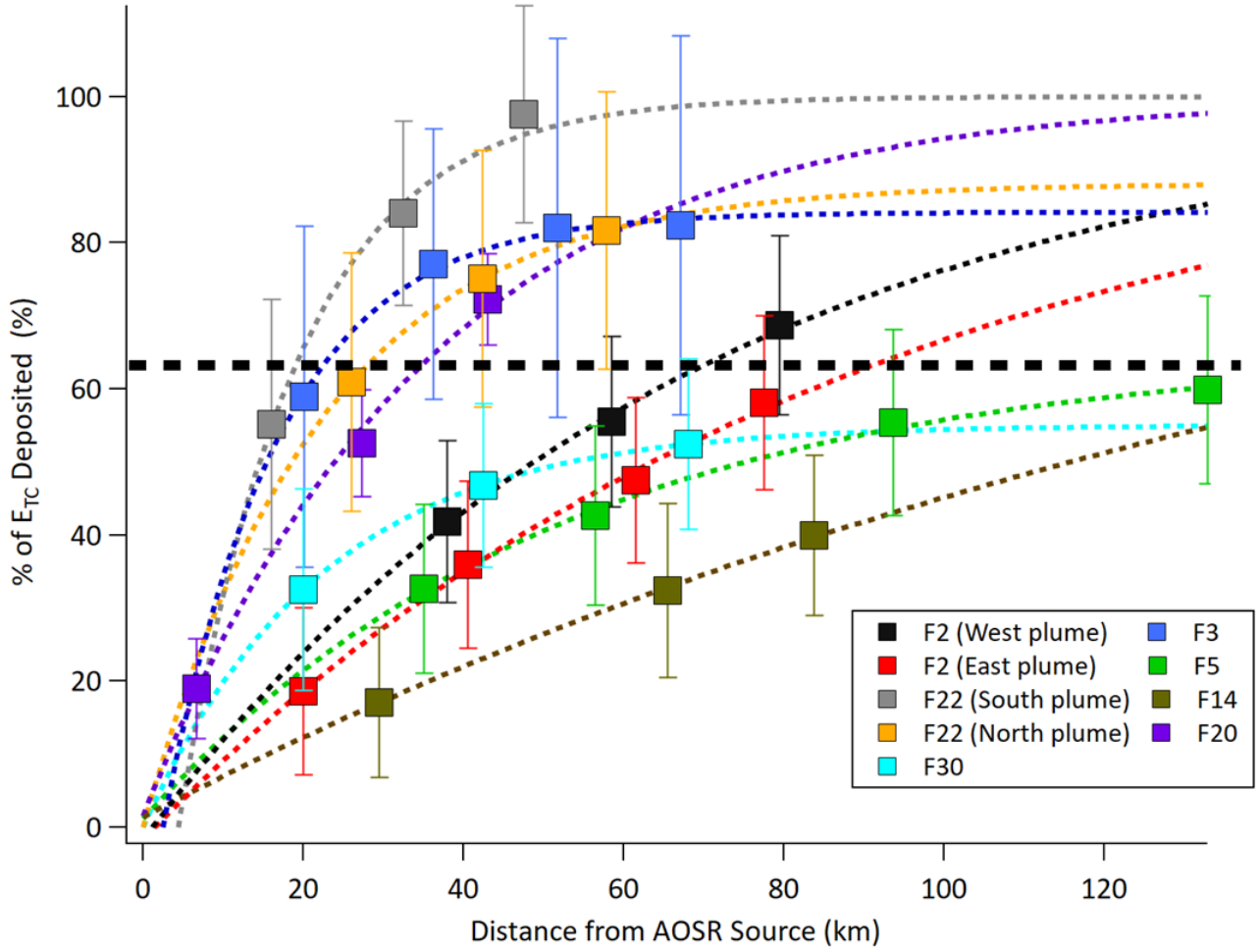

Fig. S4. Cumulative deposition normalized to the extrapolated transfer rate at source ($T_{TGOC,0}$). Coloured dashed lines represent exponential fits to the data to derive an e-folding distance (distance at which 63.2% of emissions have deposited) downwind of the Athabasca oil sands region (AOSR).

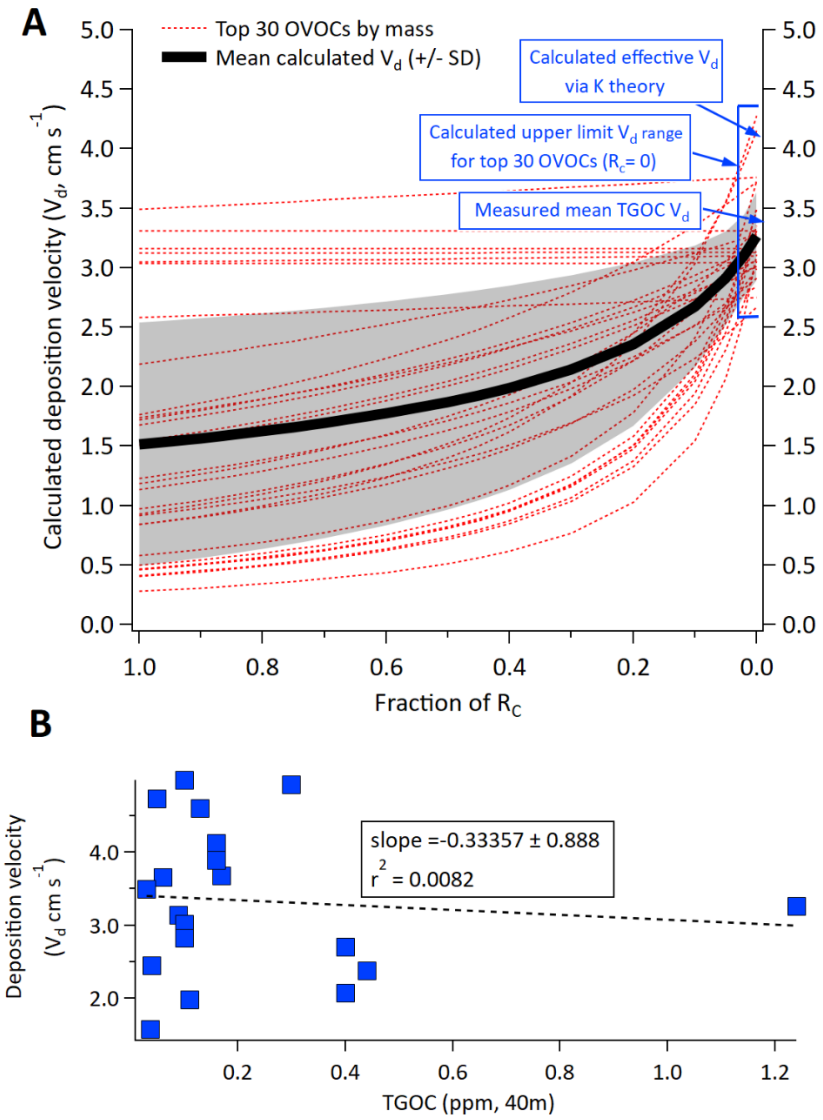

Fig. S5. Evaluating the contributions of surface resistances and absolute TGOC concentration on calculated and observed deposition velocities (V_d), respectively. (A) Calculated V_d for the top 30 OVOC species (by mass) shown as a function of decreasing surface resistance (R_c). V_d was calculated using a resistance algorithm (see main text and above) at an above canopy reference height of 40 m and surface pH=7, and for conditions representative of the oil sands region during flights. The black line represents the average and the grey region represents the standard deviation of individual estimates. The far right of the graph (i.e., fraction of R_c=0) represents the theoretical upper limit to V_d controlled only by quasi-laminar and aerodynamic resistances (R_b and R_a), shown with the measured TGOC V_d and also calculated deposition velocities without surface resistances (e.g., top 30 OVOCs and average effective V_d above surface layer from K theory; see description above), where all are similarly falling within the upper limit region. **(B)** Measured V_d and their relationship to TGOC concentration, calculated at 40 m. No discernable relationship between V_d and TGOC concentration was observed indicating observations across the flight study conditions were not dependent on the high TGOC loadings and have broader applicability to other regions.

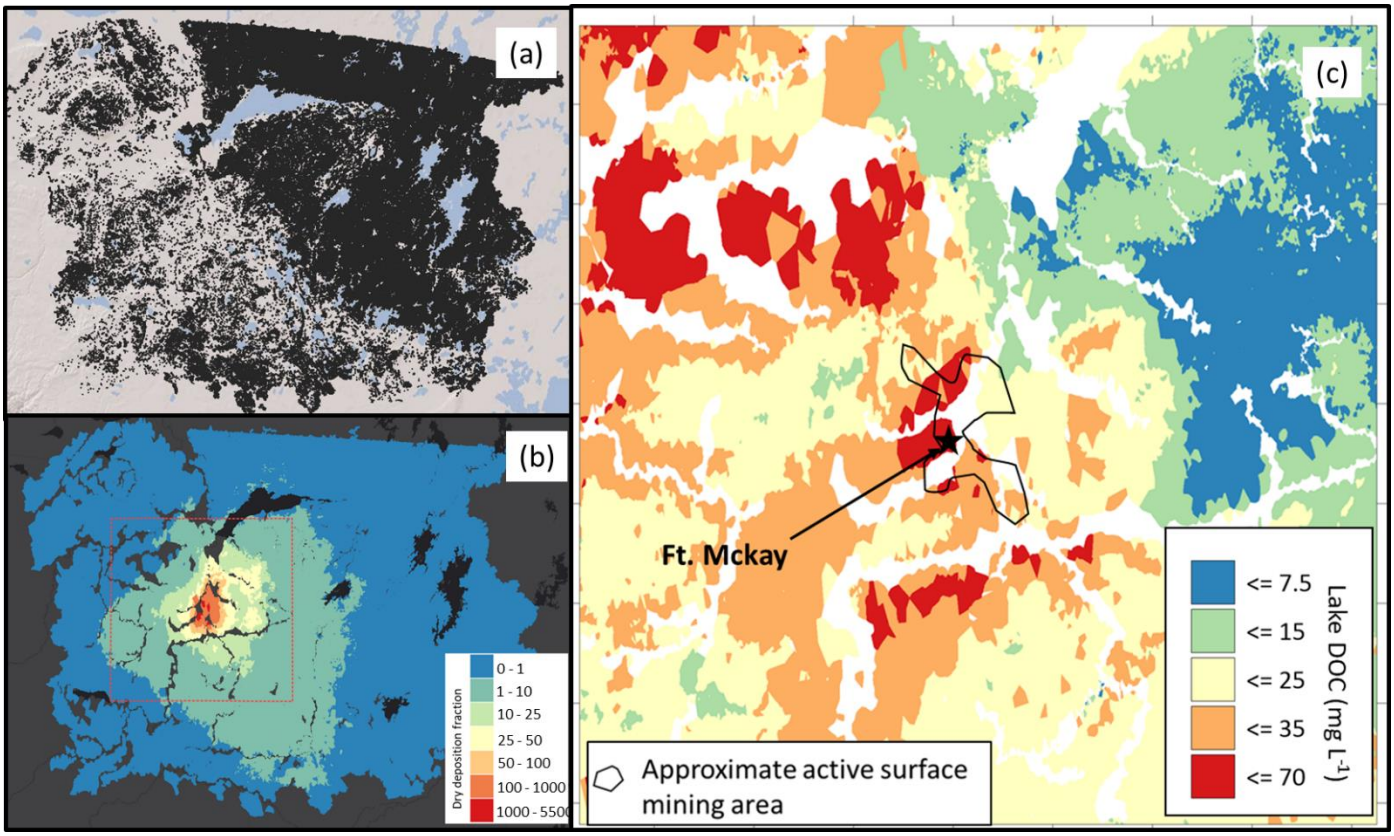

Fig. S6. Dry deposition flux ratio (DDFR) calculations. (a) Lake locations used for DDFR calculations in the study domain. **(b)** DDFR field for the entire catchment area (inset red box shows region depicted in more detail in Fig. 5(c)). **(c)** Modelled DOC concentration for the lake catchments within the sub-region shown in Fig. 5(c).

Table S1: Aircraft flights and their parameters and results used to determine TGOC dry deposition fluxes.

Flight Num.	Date	Major Upwind Facilities[a]	Total Plume foot print surface area (km^2)[b]	Mean V_d ($cm\ s^{-1}$)	Mean horizontal Wind Speed (m/s)	Mixed layer Height (m agl)	$T_{TGOC,0}$ ($t\ C\ hr^{-1}$)[c]
2 (W)	7/04/2018	SUN, SML, CNRL. MJP	3825±382	3.3±1.1	3.8	1300	71.9±7
2 (E)	7/04/2018	IKL	1238±124		3.8	1300	7.0±1
3	9/04/2018	SUN, SML	2668±267	4.9±1.1	5.1	1860	84.1±17
5	13/04/2018	SUN, SML, CNRL, MJP	5674±567	2.8±1.0	9.8	1250	49.9±5.5
14	9/06/2018	SUN, SML, CNRL, MJP	2073±207	3.9±1.2	8.9	1400	36.6±4
20	19/06/2018	SML	743±74	3.3	4.7	1500	68.7±7
22 (N)	21/06/2018	CNRL, MJP	1656±166	3.2±0.75	3.0	1200	62.5±9.4
22 (S)	21/06/2018	SUN, SML	2013±201		3.0	1200	41.8±6.3
30	5/07/2018	SUN, SML, CNRL, MJP	5167±517	2.5±0.5	6.3	1100	182±20

a. SUN = Suncor Millennium, SML = Syncrude Mildred Lake, CNRL = Canadian Natural Resources Ltd Horizon, MJP = Muskeg/Jack Pine facility, IKL = Imperial Kearl Lake. **b.** sum of surface areas below all Screens. **c.** TGOC emissions derived via extrapolation of carbon transfer rates to source (see *Application of TERRA for deposition* section, methods).

Table S2. Top 30 measured oxidized species by mass (PTRMS + CIMS) for flight 20 and associated properties used in Monte-Carlo deposition simulations

#[a]	Formula	Proposed Species[b]	$^cH_{int}$ (M/atm)	K_a	M_{diff} (cm^2/s)	f_0	α	β
1	CH_4O	methanol	$2.03x10^2$	-	0.166	0.648	0.469	0.619
2	CH_2O	formaldehyde	$3.24x10^3$	-	0.180	0	0.873	0.156
3	C_3H_6O	acetone	$2.94x10^1$	-	0.107	0	0.252	0
4	$C_4H_6O_3$	2-oxo-butanoic acid	$3.46x10^5$	$3.16x10^{-3}$	0.083	0	5.038	0
5	C_4H_6O	methacrolein	7.29	-	0.096	0.100	0.128	0.152
6	CH_2O_2	Formic acid	$8.92x10^3$	$1.77x10^{-4}$	0.127	0	2.796	0
7	C_2H_4O	acetalydehyde	13.2	-	0.124	0.100	0.177	0.171
8	$C_3H_4O_3$	pyruvic acid	$3.1x10^5$	$4.07x10^{-3}$	0.093	0	5.038	0
9	$C_2H_4O_2$	acetic acid	$4.05x10^3$	$1.75x10^{-5}$	0.124	0.100	1.975	0.152
10	$C_3H_6O_3$	Hydroxy propionic acid	$5.43x10^2$	$3.09x10^{-5}$	0.090	0.100	1.975	0.152
11	$C_4H_4O_2$	2-furanone	100	-	0.093	0.000	0.241	0.152
12	$C_5H_{10}O_3$	hydroxymethyl butyric acid	$5.0x10^3$	$2.0x10^{-5}$	0.075	0.100	1.925	0.164
13	$C_3H_6O_2$	propanoic acid	$2.25x10^3$	$1.35x10^{-5}$	0.095	0	1.955	0
14	C_4H_8O	2-butanone	20	-	0.093	0	0.252	0
15	C_3H_4O	acrolein	10	-	0.105	0.100	0.128	0.152
16	$C_4H_6O_2$	methacrylic acid	$1.9x10^3$	$4.57x10^{-5}$	0.085	0	5.038	0
17	$C_{10}H_{10}O_2$	Methylcinnamic acid	$5.0x10^4$	$2.75x10^{-5}$	0.061	0	1.955	0
18	C_5H_6O	cyclopentenone	55.2	-	0.077	0	0.241	0.152
19	$C_5H_{10}O_2$	Valeric acid	$2.3x10^3$	$1.48x10^{-5}$	0.069	0	1.955	0
20	$C_5H_8O_2$	2-Methyl-2-butenoic acid	$1.41x10^3$	$3.09x10^{-5}$	0.066	0	1.955	0
21	$C_7H_{14}O_2$	heptanoic acid	$1.7x10^3$	$1.29x10^{-5}$	0.057	0	1.955	0
22	$C_5H_6O_2$	pentadieneoic acid	$2.74x10^3$	$3.09x10^{-5}$	0.082	0	1.955	0
23	$C_5H_8O_3$	levulinic acid	$2.04x10^6$	$2.57x10^{-5}$	0.076	0	5.038	0
24	$C_3H_4O_2$	acrylic acid	$3.1x10^3$	$5.62x10^{-5}$	0.091	0	5.038	0
25	$C_6H_{10}O_2$	cyclopentanoic acid	$1.33x10^3$	$1.02x10^{-5}$	0.074	0	1.955	0
26	$C_4H_8O_2$	butanoic acid	$4.7x10^3$	$1.48x10^{-5}$	0.078	0	1.955	0
27	$C_6H_4O_2$	benzoquinone	2.1	-	0.080	0	0.241	0.152
28	$C_4H_7NO_5$	MVK hydroxy nitrate	$6.0x10^3$	-	0.075	7.101	0.214	0
29	$C_5H_4O_3$	2-furancarboxyllic acid	$9.26x10^3$	$6.92x10^{-4}$	0.080	0	1.955	0
30	$C_4H_8O_3$	3-Hydroxybutanoic acid	$1.98x10^6$	$2.0x10^{-5}$	0.081	0	1.955	0

a. Numbers correspond to those in Fig. 3a. **b.** Multiple different species are possible in some instances. Compounds listed generally represent the species used in instrument calibrations. The top 30 species for flight 20 are also very similar to those of other oil sands flights given the

similarity of precursor emissions. **c.** The H_{int} value only applies to organic acid species. For non-acidic species the value represents the effective Henry Law constant (After hydrolysis of aldehydes if applicable). Values of H_{int} and K_a, were extracted from the available literature (*107, 108*) and references therein or calculated with group contribution methods (*109*). Molecular diffusivity (M_{diff}) derived using group methods (EPA On-line Tools for Site Assessment Calculation | Ecosystems Research | US EPA). f_0, α and β terms are proxies for reactivity or the degree of similarity of the depositing chemical to either SO_2 (α) or O_3 (β) as described elsewhere (*9*)

Table S3: Estimated OH radical rate constants (k_{OH}) used to derive lifetime estimates for adsorbent tube data (IVOC/SVOC volatility range) as a function of carbon number and double bond equivalency (DBE)

	n-alkanes	**cyclic alkanes[a]**			**Single-ring aromatics[b]**			**PACs[c]**								
Carbon #	***DBE 0***	***DBE 1***	***DBE 2***	***DBE 3***	***DBE 4***	***DBE 5***	***DBE 6***	***DBE 7***	***DBE 8***	***DBE 9***	***DBE 10***	***DBE 11***	***DBE 12***	***DBE 13***	***DBE 14***	***DBE 15***
10	1.10E-11	1.48E-11	1.85E-11	2.29E-11	1.76E-11	1.10E-11		2.16E-11								
11	1.25E-11	1.62E-11	1.51E-11	2.46E-11	9.21E-12	2.07E-11		5.65E-11								
12	1.32E-11	1.76E-11	2.14E-11	2.63E-11	3.32E-11	4.56E-11	2.20E-11	6.94E-11	6.69E-11							
13	1.53E-11	1.91E-11	2.30E-11	2.80E-11	3.33E-11	2.55E-11	1.64E-11	1.24E-10	6.59E-11	8.85E-12						
14	1.67E-11	2.05E-11	2.42E-11	2.97E-11	3.29E-11	1.87E-11	2.06E-11	2.01E-10	1.16E-10	9.56E-12	4.00E-11					
15	1.81E-11	2.19E-11	2.56E-11	2.62E-11	1.49E-11	1.71E-11	5.70E-11	2.01E-10	2.03E-10	1.89E-11	1.05E-10					
16	1.94E-11	2.33E-11	2.70E-11	2.79E-11	2.56E-11	1.88E-11	6.77E-11	2.01E-10	2.03E-10	3.36E-11	3.34E-11	4.17E-11	5.00E-11			
17	2.10E-11	2.47E-11	2.84E-11	2.97E-11	1.79E-11	1.94E-11	1.67E-11	2.01E-10	2.03E-10	4.83E-11	7.48E-11	7.28E-11	1.31E-10			
18	2.24E-11	2.61E-11	2.98E-11	3.16E-11	5.27E-11	2.13E-11	2.56E-11	2.01E-10	2.03E-10	5.38E-11	1.34E-10	1.26E-10	1.60E-10	5.00E-11		
19	2.38E-11	2.75E-11	3.12E-11	3.34E-11	2.09E-11	2.37E-11	2.97E-11	6.46E-11	2.03E-10	5.93E-11	2.01E-10	2.03E-10	2.00E-10	1.31E-10	1.52E-10	
20	2.52E-11	2.90E-11	3.26E-11	3.52E-11	6.34E-11	3.53E-11	3.81E-11	7.60E-11	2.04E-10	7.27E-11	2.01E-10	2.03E-10	2.01E-10	1.60E-10	2.01E-10	5.00E-11
21	2.66E-11	3.04E-11	3.40E-11	3.66E-11	4.58E-11	2.65E-11	3.27E-11	6.74E-11	2.05E-10	8.62E-11	2.01E-10	2.03E-10	2.01E-10	2.00E-10	2.01E-10	1.31E-10
22	2.81E-11	3.18E-11	3.54E-11	3.80E-11	2.50E-11	3.56E-11	2.06E-11	2.08E-10	2.07E-10	8.60E-11	2.01E-10	2.03E-10	2.01E-10	2.01E-10	2.01E-10	1.60E-10
23	2.95E-11	3.32E-11	3.68E-11	3.95E-11	2.71E-11	3.90E-11	3.47E-11	2.10E-10	2.08E-10	8.49E-11	2.01E-10	2.03E-10	2.01E-10	2.01E-10	2.01E-10	2.00E-10
24		3.46E-11	3.82E-11	4.09E-11	2.85E-11	3.23E-11	4.03E-11	2.08E-10	2.09E-10	8.39E-11	2.01E-10	2.03E-10	2.01E-10	2.01E-10	2.02E-10	2.01E-10
25		3.60E-11	3.96E-11	4.23E-11	2.99E-11	3.04E-11	3.47E-11	2.09E-10	2.11E-10	8.99E-11	2.02E-10	2.04E-10	2.01E-10	2.01E-10	2.02E-10	2.01E-10

a. Assumed to be a series of C_6 rings with methyl, ethyl, butyl substituents as required. **b.** Assumed as C_6 aromatic with additional ring C_6 ring structures and substituents as required. **c.** Assumed to be a PAC backbone with additional substituents as required. Initial PAC

backbone structures (first entry in each column) follow the order of naphthalene, acenapthene, fluorine, anthracene, dihydropyrene, pyrene, chrysene, Benzo(cd)pyrene, benzo(a)pyrene. All k_{OH} values are in units of cm^3 $molecule^{-1}$ s^{-1} and estimated using group contribution methods (*80*)

Table S4. Absorptive deposition parameters used in the assessment of deposition flux and sensitivity of these parameters on the final deposition flux calculated

Deposition parameter name	**Value chosen**	**Sensitivity range investigated**	**Relative effect of the sensitivity range on total carbon deposition flux**	**Notes**
Molecular weight of substrate organic material (MW_{OM} : g mole^{-1})	352.68	250-400	±7%	Assuming n-pentacosane
Molar Volume of (MV : cm^3 mole^{-1})	453	300-600	±6%	n-pentacosane MV = MW/density
Fraction organic material in substrate (f_{OM})	1	NA	NA	The substrate is only organic, hence = 1
Activity coefficient (ς_i)	1	0.5 - 1	±10%	
Leaf Area Index (LAI : m^2 Leaf m^{-2} ground)	3	1-3	±15%	
Canopy Depth (D_{canopy} : m)	30	20-40	±10%	
Substrate Mass (Sub_m :µgm^{-3})	Range	200 – 1x10^6	Factor of 2	See Fig. 3b
Vapor Pressure ($p^0_{L,i}$; Torr)	Range between C10-C32 species	NA	Factor 2	Estimated for all IVOC/SVOC using a group contribution method (SIMPOL)(*120*) and an empirical relationship method (Makar et al, 2001)(*119*)
Concentration of IVOC/SVOC (observational evidence for high molecular mass compounds) (µgm^{-3})	NA	Several flight measurements (See Fig. 3b)	Factor of 7	Concentration measured during flight screens in 3 different flights (see Fig. 3b).

Table S5. Measured TGOC:NO_x emission ratios used as emissions input in the GEM-MACH model

Facility Name	Acronym	Facility Type	Average Measured TGOC Emissions (tonnes C hr^{-1})	Average Measured Hourly NOx (as NO_2) Emissions (TERRA; tonnes hr^{-1})	Annual Reported NOx Emissions (kt yr^{-1})[a]	Average Emission Ratio (ER; kg C kg^{-1} NOx)[b]
Syncrude Mildred Lake	SML	Surface mines	38.5±17	2.4±0.9	20.62	24±11
Suncor	SUN	Surface mines	12.2±5	1.6±0.3	19.05	13±7
Canadian Natural Resources Ltd - Horizon	CNRL	Surface mines	9.9±3.1	0.8±0.4	9.82	17±6
CNRL Muskeg River/Jack Pine	MJP	Surface mines	5.8±1.2	NA	8.44	NA
Imperial Kearl Lake	IKL	Surface mines	4.5±1.0	0.35	5.04	22±10
Suncor - Fort Hills	SFH	Surface mines	2.5±0.5	0.28	4.3	15±8
Suncor Firebag	SFB	In-situ	7.8±1.5	0.15±0.05	2.89	60±30

[a] From NPRI and AEIR Facility-Reported Data.
[b] Average ratio based on TERRA emissions and empirical concentration correlations (He et al., 2024) (*38*). NO_x calculated as NO_2.

REFERENCES AND NOTES

1. Y. Gao, M. Ma, T. Yang, W. Chen, T. Yang, Global atmospheric sulfur deposition and associated impaction on nitrogen cycling in ecosystems. *J. Clean. Prod.* **195**, 1–9 (2018).

2. X. Zhan, Y. Bo, F. Zhou, X. Liu, H. W. Paerl, J. Shen, R. Wang, F. Li, S. Tao, Y. Dong, X. Tang, Evidence for the importance of atmospheric nitrogen deposition to Eutrophic Lake Dianchi, China. *Environ. Sci. Technol.* **51**, 6699–6708 (2017).

3. J. M. McGrath, A. M. Betzelberger, S. Wang, E. Shook, X. G. Zhu, S. P. Long, E. A. Ainsworth, An analysis of ozone damage to historical maize and soybean yields in the United States. *Proc. Natl. Acad. Sci. U.S.A.* **112**, 14390–14395 (2015).

4. T. E. Graedel, C. J. Weschler, Chemistry within aqueous atmospheric aerosols and raindrops. *Rev. Geophys.* **19**, 505–539 (1981).

5. A. Singh, M. Agrawal, Acid rain and its ecological consequences. *J. Environ. Biol.* **29**, 15–24 (2008).

6. S. M. Lyons, K. J. Hageman, Foliar photodegradation in pesticide fate modeling: Development and evaluation of the pesticide dissipation from Agricultural Land (PeDAL) model. *Environ. Sci. Technol.* **55**, 4842–4850 (2021).

7. M. Taylor, S. M. Lyons, C. L. Davie-Martin, T. S. Geoghegan, K. J. Hageman, Understanding trends in pesticide volatilization from agricultural fields using the pesticide loss via volatilization model. *Environ. Sci. Technol.* **54**, 2202–2209 (2020).

8. S. Galmarini, P. Makar, O. E. Clifton, C. Hogrefe, J. O. Bash, R. Bellasio, R. Bianconi, J. Bieser, T. Butler, J. Ducker, J. Flemming, A. Hodzic, C. D. Holmes, I. Kioutsioukis, R. Kranenburg, A. Lupascu, J. L. Perez-Camanyo, J. Pleim, Y. H. Ryu, R. San Jose, D. Schwede, S. Silva, R. Wolke, Technical note: AQMEII4 Activity 1: Evaluation of wet and dry deposition schemes as an integral part of regional-scale air quality models. *Atmos. Chem. Phys.* **21**, 15663–15697 (2021).

9. M. L. Wesely, Parameterization of surface resistances to gaseous dry deposition in regional-scale numerical models. *Atmos. Environ.* **23**, 1293–1304 (1989).

10. J. F. Pankow, An absorption model of the gas/aerosol partitioning involved in the formation of secondary organic aerosol. *Atmos. Environ.* **28**, 189–193 (1994).

11. G. Isaacman-Vanwertz, P. Massoli, R. O'Brien, C. Lim, J. P. Franklin, J. A. Moss, J. F. Hunter, J. B. Nowak, M. R. Canagaratna, P. K. Misztal, C. Arata, J. R. Roscioli, S. T. Herndon, T. B. Onasch, A. T. Lambe, J. T. Jayne, L. Su, D. A. Knopf, A. H. Goldstein, D. R. Worsnop, J. H. Kroll, Chemical evolution of atmospheric organic carbon over multiple generations of oxidation. *Nat. Chem.* **10**, 462–468 (2018).

12. J. F. Hunter, D. A. Day, B. B. Palm, R. L. N. Yatavelli, A. W. H. Chan, L. Kaser, L. Cappellin, P. L. Hayes, E. S. Cross, A. J. Carrasquillo, P. Campuzano-Jost, H. Stark, Y. Zhao, T. Hohaus, J. N. Smith, A. Hansel, T. Karl, A. H. Goldstein, A. Guenther, D. R. Worsnop, J. A. Thornton, C. L. Heald, J. L. Jimenez, J. H. Kroll, Comprehensive characterization of atmospheric organic carbon at a forested site. *Nat. Geosci.* **10**, 748–753 (2017).

13. K. Li, J. J. B. Wentzell, Q. Liu, A. Leithead, S. G. Moussa, M. J. Wheeler, C. Han, P. Lee, S. M. Li, J. Liggio, Evolution of atmospheric total organic carbon from petrochemical mixtures. *Environ. Sci. Technol.* **55**, 12841–12851 (2021).

14. Z. Peng, J. Lee-Taylor, H. Stark, J. J. Orlando, B. Aumont, J. L. Jimenez, Evolution of OH reactivity in NO-free volatile organic compound photooxidation investigated by the fully explicit GECKO-A model. *Atmos. Chem. Phys.* **21**, 14649–14669 (2021).

15. C. L. Heald, J. H. Kroll, The fuel of atmospheric chemistry: Toward a complete description of reactive organic carbon. *Sci. Adv.* **6**, eaay8967 (2020).

16. T. Karl, P. Harley, L. Emmons, B. Thornton, A. Guenther, C. Basu, A. Turnipseed, K. Jardine, Efficient atmospheric cleansing of oxidized organic trace gases by vegetation. *Science* **330**, 816–819 (2010).

17. T. B. Nguyen, J. D. Crounse, A. P. Teng, J. M. S. Clair, F. Paulot, G. M. Wolfe, P. O. Wennberg, Rapid deposition of oxidized biogenic compounds to a temperate forest. *Proc. Natl. Acad. Sci. U.S.A.* **112**, E392–E401 (2015).

18. A. Hodzic, B. Aumont, C. Knote, J. Lee-Taylor, S. Madronich, G. Tyndall, Volatility dependence of Henry's law constants of condensable organics: Application to estimate depositional loss of secondary organic aerosols. *Geophys. Res. Lett.* **41**, 4795–4804 (2014).

19. B. Bessagnet, C. Seigneur, L. Menut, Impact of dry deposition of semi-volatile organic compounds on secondary organic aerosols. *Atmos. Environ.* **44**, 1781–1787 (2010).

20. J. M. Kelly, R. M. Doherty, F. M. O'Connor, G. W. Mann, H. Coe, D. Liu, The roles of volatile organic compound deposition and oxidation mechanisms in determining secondary organic aerosol production: A global perspective using the UKCA chemistry-climate model (vn8.4). *Geosci. Model Dev.* **12**, 2539–2569 (2019).

21. C. Bi, G. Isaacman-VanWertz, Estimated timescales for wet deposition of organic compounds as a function of Henry's law constants. *Environ. Sci. Atmos.* **2**, 1526–1533 (2022).

22. J. H. Park, A. H. Goldstein, J. Timkovsky, S. Fares, R. Weber, J. Karlik, R. Holzinger, Active atmosphere-ecosystem exchange of the vast majority of detected volatile organic compounds. *Science* **341**, 643–647 (2013).

23. M. P. Vermeuel, D. B. Millet, D. K. Farmer, M. A. Pothier, M. F. Link, M. Riches, S. Williams, L. A. Garofalo, Closing the reactive carbon flux budget: Observations from dual mass spectrometers over a coniferous forest. *J. Geophys. Res. Atmos.* **128**, (2023).

24. D. B. Millet, H. D. Alwe, X. Chen, M. J. Deventer, T. J. Griffis, R. Holzinger, S. B. Bertman, P. S. Rickly, P. S. Stevens, T. Léonardis, N. Locoge, S. Dusanter, G. S. Tyndall, S. L. Alvarez, M. H. Erickson, J. H. Flynn, Bidirectional ecosystem-atmosphere fluxes of volatile organic compounds across the mass spectrum: How many matter? *ACS Earth. Space. Chem.* **2**, 764–777 (2018).

25. E. M. Smith, Y. T. Prairie, Bacterial metabolism and growth efficiency in lakes: The importance of phosphorus availability. *Limnol. Oceanogr.* **49**, 137–147 (2004).

26. G. W. Kling, G. W. Kipphut, M. C. Miller, Arctic lakes and streams as gas conduits to the atmosphere: Implications for tundra carbon budgets. *Science* **251**, 298–301 (1991).

27. E. S. Kritzberg, E. M. Hasselquist, M. Škerlep, S. Löfgren, O. Olsson, J. Stadmark, S. Valinia, L. A. Hansson, H. Laudon, Browning of freshwaters: Consequences to ecosystem services, underlying drivers, and potential mitigation measures. *Ambio* **49**, 375–390 (2020).

28. I. F. Creed, A. K. Bergström, C. G. Trick, N. B. Grimm, D. O. Hessen, J. Karlsson, K. A. Kidd, E. Kritzberg, D. M. McKnight, E. C. Freeman, O. E. Senar, A. Andersson, J. Ask, M. Berggren, M. Cherif, R. Giesler, E. R. Hotchkiss, P. Kortelainen, M. M. Palta, T. Vrede, G. A. Weyhenmeyer, Global change-driven effects on dissolved organic matter composition: Implications for food webs of northern lakes. *Glob. Change Biol.* **24**, 3692–3714 (2018).

29. M. Erlandsson, N. Cory, S. Köhler, K. Bishop, Direct and indirect effects of increasing dissolved organic carbon levels on pH in lakes recovering from acidification. *J. Geophys. Res. Biogeo.* **115**, doi.org/10.1029/2009JG001082 (2010).

30. J. C. Summers, J. Kurek, J. L. Kirk, D. C. G. Muir, X. Wang, J. A. Wiklund, C. A. Cooke, M. S. Evans, J. P. Smol, Recent warming, rather than industrial emissions of bioavailable nutrients, is the dominant driver of lake primary production shifts across the Athabasca Oil Sands Region. *PLOS ONE* **11**, e0153987 (2016).

31. B. D. Hall, R. H. Hesslein, C. A. Emmerton, S. N. Higgins, P. Ramlal, M. J. Paterson, Multidecadal carbon sequestration in a headwater boreal lake. *Limnol. Oceanogr.* **64**, S150–S165 (2019).

32. E. Einola, M. Rantakari, P. Kankaala, P. Kortelainen, A. Ojala, H. Pajunen, S. Mäkelä, L. Arvola, Carbon pools and fluxes in a chain of five boreal lakes: A dry and wet year comparison. *J. Geophys. Res. Biogeo.* **116**, doi.org/10.1029/2010jg001636 (2011).

33. P. C. Hanson, I. Buffam, J. A. Rusak, E. H. Stanley, C. Watras, Quantifying lake allochthonous organic carbon budgets using a simple equilibrium model. *Limnol. Oceanogr.* **59**, 167–181 (2014).

34. I. M. McCullough, H. A. Dugan, K. J. Farrell, A. M. Morales-Williams, Z. Ouyang, D. Roberts, F. Scordo, S. L. Bartlett, S. M. Burke, J. P. Doubek, F. E. Krivak-Tetley, N. K. Skaff, J. C. Summers, K. C. Weathers, P. C. Hanson, Dynamic modeling of organic carbon fates in lake ecosystems. *Ecol. Model.* **386**, 71–82 (2018).

35. M. Priestley, T. J. Bannan, M. Le Breton, S. D. Worrall, S. Kang, I. Pullinen, S. Schmitt, R. Tillmann, E. Kleist, D. Zhao, J. Wildt, O. Garmash, A. Mehra, A. Bacak, D. E. Shallcross, A. Kiendler-Scharr, A. M. Hallquist, M. Ehn, H. Coe, C. J. Percival, M. Hallquist, T. F. Mentel, G. McFiggans, Chemical characterisation of benzene oxidation products under high- and low-NOx conditions using chemical ionisation mass spectrometry. *Atmos. Chem. Phys.* **21**, 3473–3490 (2021).

36. G. I. Ågren, D. B. Kleja, E. Bosatta, Modelling dissolved organic carbon production in coniferous forest soils. *Soil Sci. Soc. Am. J.* **82**, 1392–1403 (2018).

37. K. Hayden, S. M. Li, P. Makar, J. Liggio, S. G. Moussa, A. Akingunola, R. McLaren, R. M. Staebler, A. Darlington, J. O'Brien, J. Zhang, M. Wolde, L. Zhang, New methodology shows short atmospheric lifetimes of oxidized sulfur and nitrogen due to dry deposition. *Atmos. Chem. Phys.* **21**, 8377–8392 (2021).

38. M. He, J. C. Ditto, L. Gardner, J. Machesky, T. N. Hass-Mitchell, C. H. Chen, P. Khare, B. Sahin, J. D. Fortner, D. L. Plata, B. D. Drollette, K. Hayden, J. Wentzell, R. L. Mittermeier, A. Leithead, P. Lee, A. Darlington, J. Zhang, S. N. Wren, M. Wolde, S. G. Moussa, S.-M. Li, J. Liggio, D. R. Gentner, Total organic carbon measurements reveal major gaps in petrochemical emissions reporting. *Science* **383**, 426–432 (2024).

39. J. Liggio, S. G. Moussa, J. Wentzell, A. Darlington, P. Liu, A. Leithead, K. Hayden, J. O'Brien, R. L. Mittermeier, R. Staebler, M. Wolde, S. M. Li, Understanding the primary emissions and secondary formation of gaseous organic acids in the oil sands region of Alberta, Canada. *Atmos. Chem. Phys.* **17**, 8411–8427 (2017).

40. M. Gordon, S. M. Li, R. Staebler, A. Darlington, K. Hayden, J. O'Brien, M. Wolde, Determining air pollutant emission rates based on mass balance using airborne measurement data over the Alberta oil sands operations. *Atmos. Meas. Tech.* **8**, 3745–3765 (2015).

41. J. Liggio, S. M. Li, K. Hayden, Y. M. Taha, C. Stroud, A. Darlington, B. D. Drollette, M. Gordon, P. Lee, P. Liu, A. Leithead, S. G. Moussa, D. Wang, J. O'Brien, R. L. Mittermeier, J. R. Brook, G. Lu, R. M. Staebler, Y. Han, T. W. Tokarek, H. D. Osthoff, P. A. Makar, J. Zhang, D. L. Plata, D. R. Gentner, Oil sands operations as a large source of secondary organic aerosols. *Nature* **534**, 91–94 (2016).

42. J. Liggio, C. A. Stroud, J. J. B. Wentzell, J. Zhang, J. Sommers, A. Darlington, P. S. K. Liu, S. G. Moussa, A. Leithead, K. Hayden, R. L. Mittermeier, R. Staebler, M. Wolde, S. M. Li, Quantifying the primary emissions and photochemical formation of Isocyanic acid downwind of oil sands operations. *Environ. Sci. Technol.* **51**, 14462–14471 (2017).

43. S. M. Li, A. Leithead, S. G. Moussa, J. Liggio, M. D. Moran, D. Wang, K. Hayden, A. Darlington, M. Gordon, R. Staebler, P. A. Makar, C. A. Stroud, R. McLaren, P. S. K. Liu, J. O'Brien, R. L. Mittermeier, J. Zhang, G. Marson, S. G. Cober, M. Wolde, J. J. B. Wentzell, Differences between measured and reported volatile organic compound emissions from oil sands facilities in Alberta, Canada. *Proc. Natl. Acad. Sci. U.S.A.* **114**, E3756–E3765 (2017).

44. P. A. Makar, C. Stroud, J. Zhang, M. Moran, A. Akingunola, W. Gong, S. Gravel, B. Pabla, P. Cheung, Q. Zheng, G. Marson, S. M. Li, J. Brook, K. Hayden, J. Liggio, R. Staebler, A. Darlington, "High resolution model simulations of the Canadian oil sands with comparisons to field study observations" in *Air Pollution Modeling and its Application XXIV*, Springer Proceedings in Complexity, D. G. Steyn, N. Chaumerliac, Eds. (Springer Cham, 2016), pp. 503–508.

45. W. P. L. Carter, G. Heo, Development of revised SAPRC aromatics mechanisms. *Atmos. Environ.* **77**, 404–414 (2013).

46. P. A. Makar, A. Akingunola, J. Aherne, A. S. Cole, Y. A. Aklilu, J. Zhang, I. Wong, K. Hayden, S. M. Li, J. Kirk, K. Scott, M. D. Moran, A. Robichaud, H. Cathcart, P. Baratzedah, B. Pabla, P. Cheung, Q. Zheng, D. S. Jeffries, Estimates of exceedances of critical loads for

acidifying deposition in Alberta and Saskatchewan. *Atmos. Chem. Phys.* **18**, 9897–9927 (2018).

47. L. I. Kleinman, S. R. Springston, P. H. Daum, Y.-N. Lee, L. J. Nunnermacker, G. I. Senum, J. Wang, J. Weinstein-Lloyd, M. L. Alexander, J. Hubbe, J. Ortega, M. R. Canagaratna, J. Jayne, The time evolution of aerosol composition over the Mexico City plateau. *Atmos. Chem. Phys.* **8**, 1559–1575 (2008).

48. C. J. Weschler, W. W. Nazaroff, Semivolatile organic compounds in indoor environments. *Atmos. Environ.* **42**, 9018–9040 (2008).

49. P. Kömp, M. S. McLachlan, Interspecies variability of the plant/air partitioning of polychlorinated biphenyls. *Environ. Sci. Technol.* **31**, 2944–2948 (1997).

50. C. H. Whaley, P. A. Makar, M. W. Shephard, L. Zhang, J. Zhang, Q. Zheng, A. Akingunola, G. R. Wentworth, J. G. Murphy, S. K. Kharol, K. E. Cady-Pereira, Contributions of natural and anthropogenic sources to ambient ammonia in the Athabasca Oil Sands and North-Western Canada. *Atmos. Chem. Phys.* **18**, 2011–2034 (2018).

51. D. R. Oros, L. J. Standley, X. Chen, B. R. T. Simoneit, Epicuticular wax compositions of predominant conifers of western North America. *Z. Naturforsch. Sect. C J. Biosci* **54**, 17–24 (1999).

52. C. R. Kroptavich, S. Zhou, S. F. Kowal, T. F. Kahan, Physical and chemical characterization of urban grime sampled from two cities. *ACS Earth Space Chem.* **4**, 1813–1822 (2020).

53. A. M. Baergen, D. J. Donaldson, Seasonality of the water-soluble inorganic Ion composition and water uptake behavior of urban grime. *Environ. Sci. Technol.* **53**, 5671–5677 (2019).

54. B. T. Jobson, G. J. Frost, S. A. McKeen, T. B. Ryerson, M. P. Buhr, D. D. Parrish, M. Trainer, F. C. Fehsenfeld, Hydrogen peroxide dry deposition lifetime determined from observed loss rates in a power plant plume. *J. Geophys. Res. Atmos.* **103**, 22617–22628 (1998).

55. M. P. Vermeuel, G. A. Novak, C. M. Jernigan, T. H. Bertram, Diel profile of hydroperoxymethyl thioformate: Evidence for surface deposition and multiphase chemistry. *Environ. Sci. Technol.* **54**, 12521–12529 (2020).

56. J. C. Ditto, M. He, T. N. Hass-Mitchell, S. G. Moussa, K. Hayden, S. M. Li, J. Liggio, A. Leithead, P. Lee, M. J. Wheeler, J. J. B. Wentzell, D. R. Gentner, Atmospheric evolution of emissions from a boreal forest fire: The formation of highly functionalized oxygen-, nitrogen-, and sulfur-containing organic compounds. *Atmos. Chem. Phys.* **21**, 255–267 (2021).

57. A. Hodzic, P. S. Kasibhatla, D. S. Jo, C. D. Cappa, J. L. Jimenez, S. Madronich, R. J. Park, Rethinking the global secondary organic aerosol (SOA) budget: Stronger production, faster removal, shorter lifetime. *Atmos. Chem. Phys.* **16**, 7917–7941 (2016).

58. G. Isaacman-Vanwertz, B. Aumont, Impact of organic molecular structure on the estimation of atmospherically relevant physicochemical parameters. *Atmos. Chem. Phys.* **21**, 6541–6563 (2021).

59. C. Knote, A. Hodzic, J. L. Jimenez, The effect of dry and wet deposition of condensable vapors on secondary organic aerosols concentrations over the continental US. *Atmos. Chem. Phys.* **15**, 1–18 (2015).

60. H. Cathcart, J. Aherne, D. S. Jeffries, K. A. Scott, Critical loads of acidity for 90,000 lakes in northern Saskatchewan: A novel approach for mapping regional sensitivity to acidic deposition. *Atmos. Environ.* **146**, 290–299 (2016).

61. S. Sobek, B. Söderbäck, S. Karlsson, E. Andersson, A. K. Brunberg, A carbon budget of a small humic lake: An example of the importance of lakes for organic matter cycling in boreal catchments. *Ambio* **35**, 469–475 (2006).

62. P. J. Dillon, L. A. Molot, The role of ammonium and nitrate retention in the acidification of lakes and forested catchments. *Biogeochemistry* **11**, 23–43 (1990).

63. Y. Liu, Y. Huang, J. Liggio, K. Hayden, C. Mihele, J. Wentzell, M. Wheeler, A. Leithead, S. Moussa, C. Xie, Y. Yang, Y. Zhang, T. Han, S. M. Li, A newly developed Lagrangian chemical transport scheme: Part 1. Simulation of a boreal forest fire plume. *Sci. Total Environ.* **880**, 163232 (2023).

64. D. Blanchard, J. Aherne, P. Makar, Dissolved organic carbon in lakes of the Athabasca oil sands region: Is color an indicator of acid sensitivity? *Environ. Sci. Technol.* **55**, 6791–6803 (2021).

65. S. Heyen, B. M. Scholz-Böttcher, R. Rabus, H. Wilkes, Release of carboxylic acids into the exometabolome during anaerobic growth of a denitrifying bacterium with single substrates or crude oil. *Org. Geochem.* **154**, 104179 (2021).

66. M. Rodrigue, V. Elango, D. Curtis, A. W. Collins, J. H. Pardue, Biodegradation of MC252 polycyclic aromatic hydrocarbons and alkanes in two coastal wetlands. *Mar. Pollut. Bull.* **157**, 111319 (2020).

67. J. F. Lapierre, F. Guillemette, M. Berggren, P. A. Del Giorgio, Increases in terrestrially derived carbon stimulate organic carbon processing and CO_2 emissions in boreal aquatic ecosystems. *Nat. Commun.* **4**, 2972 (2013).

68. D. A. Seekell, J. F. Lapierre, J. Ask, A. K. Bergstreom, A. Deininger, P. Rodriguez, J. Karlsson, The influence of dissolved organic carbon on primary production in northern lakes. *Limnol. Oceanogr.* **60**, 1276–1285 (2015).

69. J. Kurek, J. L. Kirk, D. C. G. Muir, X. Wang, M. S. Evans, J. P. Smol, Legacy of a half century of Athabasca oil sands development recorded by lake ecosystems. *Proc. Natl. Acad. Sci. U.S.A.* **110**, 1761–1766 (2013).

70. Y. Li, C. Fu, L. Zeng, Q. Zhou, H. Zhang, C. Tu, L. Li, Y. Luo, Black carbon contributes substantially to allochthonous carbon storage in deltaic vegetated coastal habitats. *Environ. Sci. Technol.* **55**, 6495–6504 (2021).

71. G. M. Lovett, S. E. Lindberg, Atmospheric deposition and canopy interactions of nitrogen in forests. *Can. J. For. Res.* **23**, 1603–1616 (1993).

72. K. L. Hayden, S. M. Li, J. Liggio, M. J. Wheeler, J. J. B. Wentzell, A. Leithead, P. Brickell, R. L. Mittermeier, Z. Oldham, C. M. Mihele, R. M. Staebler, S. G. Moussa, A. Darlington, M. Wolde, D. Thompson, J. Chen, D. Griffin, E. Eckert, J. C. Ditto, M. He, D. R. Gentner, Reconciling the total carbon budget for boreal forest wildfire emissions using airborne observations. *Atmos. Chem. Phys.* **22**, 12493–12523 (2022).

73. C. E. Stockwell, A. Kupc, B. Witkowski, R. K. Talukdar, Y. Liu, V. Selimovic, K. J. Zarzana, K. Sekimoto, C. Warneke, R. A. Washenfelder, R. J. Yokelson, A. M. Middlebrook, J. M. Roberts, Characterization of a catalyst-based conversion technique to measure total particulate nitrogen and organic carbon and comparison to a particle mass measurement instrument. *Atmos. Meas. Tech.* **11**, 2746–2764 (2018).

74. P. Veres, J. B. Gilman, J. M. Roberts, W. C. Kuster, C. Warneke, I. R. Burling, J. De Gouw, Development and validation of a portable gas phase standard generation and calibration system for volatile organic compounds. *Atmos. Meas. Tech.* **3**, 683–691 (2010).

75. K. Li, J. Liggio, P. Lee, C. Han, Q. Liu, S.-M. Li, Secondary organic aerosol formation from α-pinene, alkanes, and oil-sands-related precursors in a new oxidation flow reactor. *Atmos. Chem. Phys.* **19**, 9715–9731 (2019).

76. J. Liggio, S. M. Li, R. M. Staebler, K. Hayden, A. Darlington, R. L. Mittermeier, J. O'Brien, R. McLaren, M. Wolde, D. Worthy, F. Vogel, Measured Canadian oil sands CO_2 emissions are higher than estimates made using internationally recommended methods. *Nat. Commun.* **10**, 1863 (2019).

77. J. A. Manion, R. E. Huie, R. D. Levin, D. R. Burgess Jr., V. L. Orkin, W. Tsang, W. S. McGivern, J. W. Hudgens, V. D. Knyazev, D. B. Atkinson, E. Chai, A. M. Tereza, C.-Y. Lin, T. C. Allison, W. G. Mallard, F. Westley, J. T. Herron, R. F. Hampson, D. H. Frizzell, *NIST Chemical Kinetics Database, NIST Standard Reference Database 17, Version 7.0 (Web Version)* (National Institute of Standards and Technology, 2015); http://kinetics.nist.gov/.

78. R. Atkinson, J. Arey, Atmospheric degradation of volatile organic compounds. *Chem. Rev.* **103**, 4605–4638 (2003).

79. N. M. Donahue, W. Chuang, S. A. Epstein, J. H. Kroll, D. R. Worsnop, A. L. Robinson, P. J. Adams, S. N. Pandis, Why do organic aerosols exist? Understanding aerosol lifetimes using the two-dimensional volatility basis set. *Environ. Chem.* **10**, 151 (2013).

80. US Environmental Protection Agency (Washington, DC, USA, 2012).

81. C. A. Stroud, P. A. Makar, J. Zhang, M. D. Moran, A. Akingunola, S. M. Li, A. Leithead, K. Hayden, M. Siu, Improving air quality model predictions of organic species using measurement-derived organic gaseous and particle emissions in a petrochemical-dominated region. *Atmos. Chem. Phys.* **18**, 13531–13545 (2018).

82. D. D. Baldocchi, B. B. Hicks, P. Camara, A canopy stomatal resistance model for gaseous deposition to vegetated surfaces. *Atmos. Environ.* **21**, 91–101 (1987).

83. J. Zhang, M. D. Moran, P. A. Makar, S. K. Kharol, paper presented at the 19th Annual CMAS Conference, Virtual, 2020.

84. S. J. Miller, P. A. Makar, C. J. Lee, HETerogeneous vectorized or Parallel (HETPv1.0): An updated inorganic heterogeneous chemistry solver for the metastable-state NH_4^+-Na^+-Ca^{2+}-K^+-Mg^{2+}-SO_4^{2-} - NO_3^- - Cl^-- H2O system based on ISORROPIA II. *Geosci. Model Dev.* **17**, 2197–2219 (2024).

85. P. A. Makar, A. Akingunola, J. Chen, B. Pabla, W. Gong, C. Stroud, C. Sioris, K. Anderson, P. Cheung, J. Zhang, J. Milbrandt, Forest-fire aerosol-weather feedbacks over western North America using a high-resolution, online coupled air-quality model. *Atmos. Chem. Phys.* **21**, 10557–10587 (2021).

86. R. Ghahreman, W. Gong, P. A. Makar, A. Lupu, A. Cole, K. Banwait, C. Lee, A. Akingunola, Modeling below-cloud scavenging of size-resolved particles in GEM-MACHv3.1. *Geosci. Model Dev.* **17**, 685–707 (2024).

87. P. A. Makar, R. M. Staebler, A. Akingunola, J. Zhang, C. McLinden, S. K. Kharol, B. Pabla, P. Cheung, Q. Zheng, The effects of forest canopy shading and turbulence on boundary layer ozone. *Nat. Commun.* **8**, 15243 (2017).

88. P. A. Makar, C. Stroud, A. Akingunola, J. Zhang, S. Ren, P. Cheung, Q. Zheng, Vehicle-induced turbulence and atmospheric pollution. *Atmos. Chem. Phys.* **21**, 12291–12316 (2021).

89. J. Zhang, M. D. Moran, Q. Zheng, P. A. Makar, P. Baratzadeh, G. Marson, P. Liu, S. M. Li, Emissions preparation and analysis for multiscale air quality modeling over the Athabasca Oil Sands Region of Alberta, Canada. *Atmos. Chem. Phys* **18**, 10459–10481 (2018).

90. M. Graus, M. Müller, A. Hansel, High resolution PTR-TOF: Quantification and formula confirmation of VOC in real time. *J. Am. Soc. Mass Spectrom.* **21**, 1037–1044 (2010).

91. A. Jordan, S. Haidacher, G. Hanel, E. Hartungen, L. Märk, H. Seehauser, R. Schottkowsky, P. Sulzer, T. D. Märk, A high resolution and high sensitivity proton-transfer-reaction time-of-flight mass spectrometer (PTR-TOF-MS). *Int. J. Mass Spectrom.* **286**, 122–128 (2009).

92. B. H. Lee, F. D. Lopez-Hilfiker, C. Mohr, T. Kurtén, D. R. Worsnop, J. A. Thornton, An iodide-adduct high-resolution time-of-flight chemical-ionization mass spectrometer: Application to atmospheric inorganic and organic compounds. *Environ. Sci. Technol.* **48**, 6309–6317 (2014).

93. K. Sekimoto, S. M. Li, B. Yuan, A. Koss, M. Coggon, C. Warneke, J. de Gouw, Calculation of the sensitivity of proton-transfer-reaction mass spectrometry (PTR-MS) for organic trace gases using molecular properties. *Int. J. Mass Spectrom.* **421**, 71–94 (2017).

94. A. R. Koss, K. Sekimoto, J. B. Gilman, V. Selimovic, M. M. Coggon, K. J. Zarzana, B. Yuan, B. M. Lerner, S. S. Brown, J. L. Jimenez, J. Krechmer, J. M. Roberts, C. Warneke, R. J. Yokelson, J. De Gouw, Non-methane organic gas emissions from biomass burning: Identification, quantification, and emission factors from PTR-ToF during the FIREX 2016 laboratory experiment. *Atmos. Chem. Phys.* **18**, 3299–3319 (2018).

95. B. M. Lerner, J. B. Gilman, K. C. Aikin, E. L. Atlas, P. D. Goldan, M. Graus, R. Hendershot, G. A. Isaacman-Vanwertz, A. Koss, W. C. Kuster, R. A. Lueb, R. J. McLaughlin, J. Peischl, D. Sueper, T. B. Ryerson, T. W. Tokarek, C. Warneke, B. Yuan, J. A. De Gouw, An improved, automated whole air sampler and gas chromatography mass spectrometry analysis system for volatile organic compounds in the atmosphere. *Atmos. Meas. Tech.* **10**, 291–313 (2017).

96. R. Sheu, A. Marcotte, P. Khare, S. Charan, J. C. Ditto, D. R. Gentner, Advances in offline approaches for chemically speciated measurements of trace gas-phase organic compounds via adsorbent tubes in an integrated sampling-to-analysis system. *J. Chromatogr. A* **1575**, 80–90 (2018).

97. P. Khare, J. Machesky, R. Soto, M. He, A. A. Presto, D. R. Gentner, Asphalt-related emissions are a major missing nontraditional source of secondary organic aerosol precursors. *Sci. Adv.* **6**, eabb9785 (2020).

98. J. L. Jimenez, J. T. Jayne, Q. Shi, C. E. Kolb, D. R. Worsnop, I. Yourshaw, J. H. Seinfeld, R. C. Flagan, X. Zhang, K. A. Smith, J. W. Morris, P. Davidovits, Ambient aerosol sampling using the Aerodyne Aerosol Mass Spectrometer. *J. Geophys. Res. Atmos.* **108**, doi. org/10.1029/2001JD001213 (2003).

99. P. F. DeCarlo, J. R. Kimmel, A. Trimborn, M. J. Northway, J. T. Jayne, A. C. Aiken, M. Gonin, K. Fuhrer, T. Horvath, K. S. Docherty, D. R. Worsnop, J. L. Jimenez, Field-deployable, high-resolution, time-of-flight aerosol mass spectrometer. *Anal. Chem.* **78**, 8281–8289 (2006).

100. J. L. Kirk, D. C. G. Muir, A. Gleason, X. Wang, G. Lawson, R. A. Frank, I. Lehnherr, F. Wrona, Atmospheric deposition of mercury and methylmercury to landscapes and waterbodies of the Athabasca oil sands region. *Environ. Sci. Technol.* **48**, 7374–7383 (2014).

101. S. G. Moussa, R. M. Staebler, Y. You, A. Leithead, M. A. Yousif, P. Brickell, J. Beck, Z. Jiang, J. Liggio, S.-M. Li, S. N. Wren, J. R. Brook, A. Darlington, S. G. Cober, Fugitive emissions of volatile organic compounds from a tailings pond in the oil sands region of Alberta. *Environ. Sci. Technol.* **55**, 12831–12840 (2021).

102. Y. You, S. G. Moussa, L. Zhang, L. Fu, J. Beck, R. M. Staebler, Quantifying fugitive gas emissions from an oil sands tailings pond with open-path Fourier transform infrared measurements. *Atmos. Meas. Tech.* **14**, 945–959 (2021).

103. Y. You, R. M. Staebler, S. G. Moussa, J. Beck, R. L. Mittermeier, Methane emission from an oil sands tailings pond: A quantitative comparison of fluxes derived by different methods. *Atmos. Meas. Tech.* **14**, 1879–1892 (2021).

104. U. Högström, Review of some basic characteristics of the atmospheric surface layer. *Bound.-Lay. Meteorol.* **78**, 215–246 (1996).

105. M. Gordon, S. M. Li, R. Staebler, A. Darlington, K. Hayden, J. O'Brien, M. Wolde, Determining air pollutant emission rates based on mass balance using airborne measurement data over the Alberta oil sands operations. *Atmos. Meas. Tech. Discuss.* **8**, 4769–4816 (2015).

106. L. Zhang, M. D. Moran, P. A. Makar, J. R. Brook, S. Gong, Modelling gaseous dry deposition in AURAMS: A unified regional air-quality modelling system. *Atmos. Environ.* **36**, 537–560 (2002).

107. R. Sander, Compilation of Henry's law constants (version 4.0) for water as solvent. *Atmos. Chem. Phys.* **15**, 4399–4981 (2015).

108. W. M. Haynes, *CRC HAndbook of Chemistry and Physics*, W. M. Haynes, Ed. (Taylor & Francis Group, Ed. 95, 2014).

109. J. Altschuh, R. Brüggemann, H. Santl, G. Eichinger, O. G. Piringer, Henry's law constants for a diverse set of organic chemicals: Experimental determination and comparison of estimation methods. *Chemosphere* **39**, 1871–1887 (1999).

110. H. K. Livingston, Cross-sectional areas of molecules adsorbed on solid surfaces. *J. Am. Chem. Soc.* **66**, 569–573 (1944).

111. A. F. Diefendorf, K. H. Freeman, S. L. Wing, H. V. Graham, Production of n-alkyl lipids in living plants and implications for the geologic past. *Geochim. Cosmochim. Acta* **75**, 7472–7485 (2011).

112. L. Lu, K. M. Ku, S. P. Palma-Salgado, A. P. Storm, H. Feng, J. A. Juvik, T. H. Nguyen, Influence of epicuticular physicochemical properties on porcine rotavirus adsorption to 24 leafy green vegetables and tomatoes. *PLOS ONE* **10**, (2015).

113. R. Maiti, H. G. Rodriguez, Biodiversity in leaf chemistry (pigments, epicuticular wax and leaf nutrients) in woody plant species in North-Eastern Mexico, a synthesis. *For. Res.* **5**, doi. org/10.4172/2168-9776.1000170 (2016).

114. R. Popek, H. Gawrońska, M. Wrochna, S. W. Gawroński, A. Sæbø, Particulate matter on foliage of 13 woody species: Deposition on surfaces and phytostabilisation in waxes – a 3-year study. *Int. J. Phytoremediation* **15**, 245–256 (2013).

115. P. Sharma, S. L. Kothari, M. S. Rathore, V. S. Gour, Properties, variations, roles, and potential applications of epicuticular wax: A review. *Turk. J. Bot.* **42**, 135–149 (2018).

116. V. Zeisler-Diehl, Y. Müller, L. Schreiber, Epicuticular wax on leaf cuticles does not establish the transpiration barrier, which is essentially formed by intracuticular wax. *J. Plant Physiol.* **227**, 66–74 (2018).

117. S. Manninen, S. Sipari, "Composition of needle epicuticular wax of Jack pine (*Pinus banksiana*) in the Oil Sands, Alberta, Canada" [Wood Buffalo Envirnomental Association (WBEA), 2013].

118. P. A. Makar, The estimation of organic gas vapour pressure. *Atmos. Environ.* **35**, 961–974 (2001).

119. J. F. Pankow, W. E. Asher, SIMPOL.1: A simple group contribution method for predicting vapor pressures and enthalpies of vaporization of multifunctional organic compounds. *Atmos. Chem. Phys.* **8**, 2773–2796 (2008).

120. R. G. Lamb, W. H. Chen, J. H. Seinfeld, Numerico-empirical analyses of atmospheric diffusion theories. *J. Atmos. Sci.* **32**, 1794–1807 (1975).

121. L. O. M. a. A. J. Ranzieri, “A consistent scheme for estimating diffusivities to be used in air quality models” (Report CA-DOT-TL-7169-3-76-32, California Department of Transportation, 1976).

122. C. C. Shir, A preliminary numerical study of atmospheric turbulent flows in the idealized planetary boundary layer. *J. Atmos. Sci.* **30**, 1327–1339 (1973).

123. X. Lee, *Fundamentals of Boundary-Layer Meteorology* (Springer, 2018).

124. C. M. Johnston, T. G. Dewald, T. R. Bondelid, B. B. Worstell, L. D. McKay, A. Rea, R. B. Moore, J. L. Goodall, Evaluation of catchment delineation methods for the medium-resolution National Hydrography Dataset (U.S. Geological Survey Scientific Investigations Report 2009–5233, U.S. Geological Survey, 2009).

125. L. T. C. Bonten, G. J. Reinds, M. Posch, A model to calculate effects of atmospheric deposition on soil acidification, eutrophication and carbon sequestration. *Environ. Model. Software* **79**, 75–84 (2016).